UNIVERSITA' DEGLI STUDI DI NAPOLI "FEDERICO II"

FACOLTA' DI SCIENZE MATEMATICHE, FISICHE E NATURALI

CORSO DI LAUREA TRIENNALE IN FISICA

COMPARATIVE STUDY OF MATERIALS TO BE USED IN A GEOMETRIC ANTI SPRING (GAS) FILTER FOR GRAVITATIONAL WAVES DETECTORS

Tesi di Laurea Triennale in Fisica

Relatori:

Prof. Rosario De Rosa (Federico II)

Prof. Leopoldo Milano (Federico II)

Dott. Riccardo De Salvo (Caltech)

Candidato:

Luigi Marchese

matricola 567/469

ANNO ACCADEMICO 2009/2010

"Voglio sapere come Dio

ha creato questo mondo.

Non mi interessano

questo o quel fenomeno,

lo spettro di questo o quell'elemento.

Voglio conoscere i suoi pensieri,

il resto è dettaglio".

A Luisa

Contents

"Setting an example

is not the main means

of influencing others;

it is the only means."

Albert Einstein

Introduction

The most fascinating prediction of Einstein's theory of the General Relativity is the existence of the Gravitational waves (GW). One of the most interesting aim of the modern physics is the construction of interferometric detectors able to detect such GW, whose dimensionless amplitude is extremely small, $h \sim 10^{-21}$. To achieve this goal, in the last ten years a worldwide network of GW interferometer detectors has been started. Much has changed since the first generation began to work, especially in the sensitivity range of the GW interferometer detectors. The two initial LIGO interferometers (USA) were designed to be sensitive to a GW signal in the frequency band 40 – 7000 Hz, while VIRGO (France – Italy) is sensitive in a wider range, from 10 to 10000 Hz. Advanced LIGO and VIRGO will have more than a factor 10 in sensitivity thus changing the bandwidth of high sensitivity. Moreover a new interferometer, LISA, the proposed space – based GW observatory, will detect GW in the range $10^{-4} - 0.1\ Hz$. When also LISA will be operating the only band not covered will be $0.1 - 10\ Hz$, unfortunately the most promising, since it corresponds to detection of GW from pulsars, coalescence and merger of intermediate mass black holes. To cover it, a proposal is going underground, but this is just only one among other fascinating projects for the third GW interferometers detectors generation. Clearly one of the major research goal for the new generation is the reduction of the noise at low frequency, which is dominated by the seismic noise. The seismic isolation system projected for these detectors is a fundamental problem in their building to improve their low frequency band sensitivity. The most helpful and adopted seismic isolation system is based

1

on the GAS (Geometric Anti Spring) filter, which, together with the EMAS (Electro Magnetic Anti Spring) filter allows the exploration of resonant frequencies below 100 mHz. Although not all the world detectors make use of these filters (Virgo make use of a different prototype, the so called "Super Attenuator"), each isolation system is based on Maraging steel blades, a precipitation hardened alloy that allows the production of creep – free blade springs. At high frequencies ($> 1\,Hz$), they show high attenuation performance, while at low frequencies anomalies have been observed. A previous work, investigating on the dissipation properties of these blades, revealed their connection with the dislocations, linear impurities, present inside their material structure. Starting from this viewpoint, the most promising idea to improve the attenuation performance, is the exploration of different materials which don't contain dislocations, such as LM001 Zr – based bulk metallic glass (LM001), a monolithic bulk – metallic glass (BMG) composed by Zr (41,2 %), Ti (13,8%), Cu (12.5%), Ni (10%) and Be (22,5%). This thesis work is a comparative study between this two materials to explore the possibility to substitute the Maraging blades still adopted with possible future LM001 blades. In fact, as I will show, the two filters, working together, will represent our personal microscopy to investigate the dissipation properties inside the materials.

In the first chapter I will develop briefly the theory of the Gravitational waves, while their detection will be the argument of the second chapter, with particular attention to LIGO and VIRGO.

The following chapters are the result of my 10 weeks experience at CALTECH (Californian Institute of Technology) during summer 2009. In the third chapter I will talk about the GAS and EMAS filters and about the theoretical model explaining the dissipation properties, while in the fourth chapter I will present the data analysis and the hysteresis tests.

Finally, in the fifth chapter I will present the results of my study and a possible future plan of work to strengthen the conclusions obtained in this work.

Introduzione

Una delle più affascinanti predizioni della teoria della Relatività Generale di Einstein è l'esistenza delle onde gravitazionali (OG), perturbazioni della metrica dello spazio − tempo che viaggiano alla velocità della luce. Uno dei principali obiettivi della fisica moderna è la rivelazione di tali onde gravitazionali (la cui ampiezza adimensionale è estremamente piccola, $h \sim 10^{-21}$) per mezzo di rivelatori interferometrici. A tal fine, negli ultimi dieci anni è stata intrapresa la costruzione di una potente rete mondiale di rivelatori interferometrici. Molto è cambiato da quando la prima generazione di tali rivelatori muoveva i primi passi, specialmente la loro banda di sensibilità. I primi due interferometri di LIGO (USA) erano stati progettati per essere sensibili ad un segnale gravitazionale nella banda di frequenza 40 − 7000 Hz, mentre il rivelatore VIRGO (Francia − Italia) possiede una più ampia banda di sensibilità, 10 − 10000 Hz. Gli Advanced VIRGO e LIGO, saranno migliorati di più di un fattore 10 nelle rispettive bande di sensibilità. Inoltre un nuovo interferometro, LISA, il primo osservatorio di onde gravitazionali costruito nello spazio, tenterà la rivelazione di Onde Gravitazionali nella banda $10^{-4} − 0.1\ Hz$. Una volta che LISA entrerà in funzione, l'unica banda di frequenze ancora scoperta sarà $0.1 − 10\ Hz$ che, sfortunatamente sembra essere la più promettente vista la possibilità di rivelare Onde Gravitazionali emesse da sorgenti quali pulsars, coalescenza e merger di buchi neri di massa intermedia. Per cercare di coprire anche questa banda ci sono ancora molte proposte. Una delle più interessanti è sicuramente la possibilità di costruire rivelatori interferometrici di terza generazione sotterranei. Inoltre una delle maggiori sfide dell' attuale attività

di ricerca per i futuri rivelatori è la riduzione del rumore a basse frequenze, ampiamente dominato dal rumore sismico. I sistemi di isolamento sismico per questi rivelatori di nuova generazione sono dunque un problema cruciale nella loro costruzione al fine di migliorare la loro banda di sensibilità a basse frequenze. Il più utilizzato sistema di isolamento sismico è basato su un filtro GAS (Geometric Anti Spring) che, unitamente ad un filtro EMAS (Electro Magnetic Anti Spring), ha reso possibile l'esplorazione di frequenze di risonanza al di sotto dei 100 mHz. Sebbene non tutti i rivelatori mondiali si servono di questi filtri (VIRGO si serve di un prototipo di isolamento sismico diverso, il cosiddetto "Super Attenuatore"), ogni sistema di isolamento sismico sviluppato fa uso di lame in acciaio Maraging, una lega che rende possibile la costruzione di molle (lame) prive di deformazioni permanenti. Ad alte frequenze ($> 1\,Hz$), suddette lame permettono alte performance di attenuazione simica, mentre a basse frequenze sono state osservate diversi comportamenti anomali.   Un precedente studio, investigando sulle proprietà dissipative all'interno di queste lame, ha rivelato che queste ultime sono dovute alla presenza delle dislocazioni, imperfezioni lineari che caratterizzano la struttura interna del materiale utilizzato per la loro costruzione. Partendo da questo punto di vista, la più promettente idea per migliorare la performance di attenuazione sismica, è lo studio di nuovi materiali che non contengano dislocazioni, come LM001 Zr – based bulk metallic glass (LM001), una lega metallica amorfa e dunque non cristallina nota come *glassy metal*,   composto da Zr (41,2 %), Ti (13,8%), Cu (12.5%), Ni(10%) and Be (22,5%). Questo lavoro di tesi è sostanzialmente un confronto fra i due materiali per varare la possibile sostituzione delle lame in Maraging attualmente utilizzate in un filtro GAS con lame fatte di LM001. Infatti, come mostrerò, i due filtri, lavorando pariteticamente, rappresentano il nostro personale microscopio per investigare le proprietà dissipative all'interno dei due materiali.

Nel primo capitolo svilupperò brevemente la teoria delle Onde Gravitazionali, mentre la loro rivelazione sarà oggetto di studio del secondo capitolo, con particolare attenzione ai rivelatori interferometrici LIGO e VIRGO.

I capitoli seguenti sono il risultato della mia esperienza di dieci settimane al CALTECH (Californian Institute of Techonology) durante l'estate 2009. Nel terzo capitolo illustrerò il meccanismo di funzionamento dei filtri GAS ed EMAS e il modello teorico circa le proprietà dissipative nei due materiali. Nel quarto invece proporrò l'analisi dei dati e i test di isteresi effettuati.

Infine nel quinto capitolo mostrerò i risultati e le conclusioni di questa tesi, presentando anche un possibile progetto di lavoro volto a rafforzare suddetti risultati.
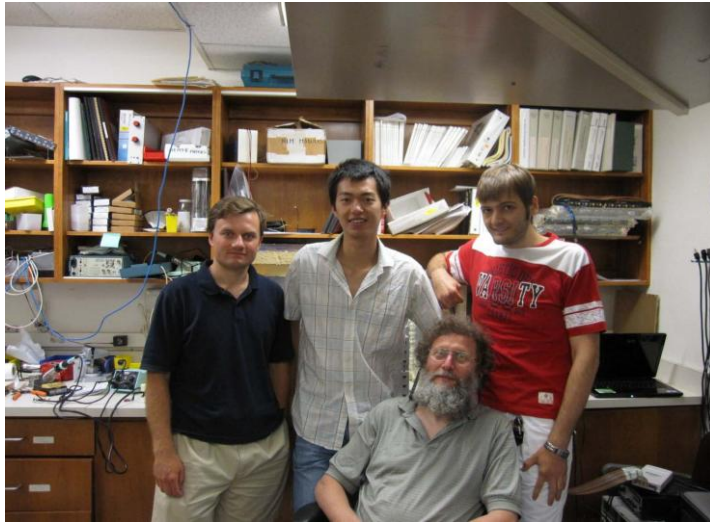
Il mio gruppo di laboratorio. Da sinistra: Andrey R. Rodionov, Gong Pu, Riccardo De Salvo
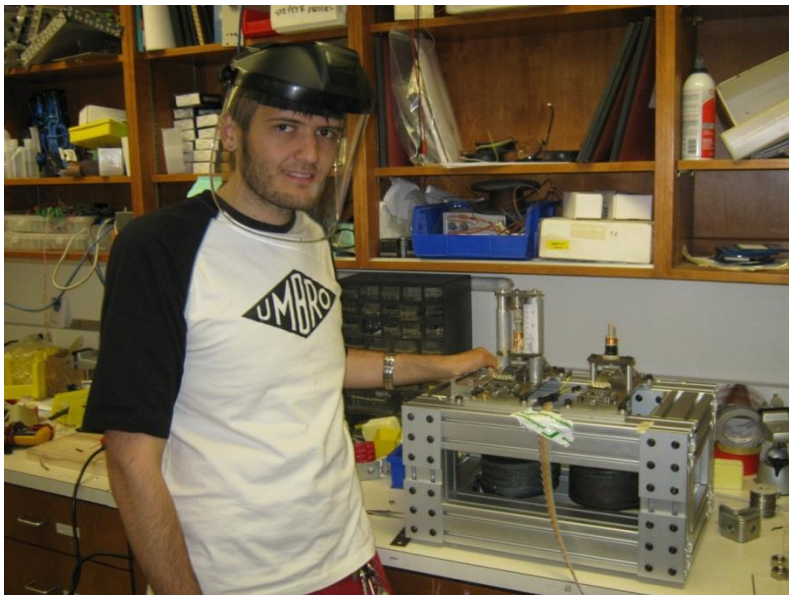
Acknowledgements

The list of people to thank is very long. First of all I want to deeply thank my supervisor at Caltech, Riccardo De Salvo, who gave me this great opportunity. He has continually and strongly supported me, teaching me a lot about physics and not. During my stay at Caltech I experienced the life of an experimental physics, from the shop machine to the laboratory activity. I found a synergistic working group with which I had a great time, in laboratory and not only. I'll never forget the Wednesday at the Six Flags with all my working group.

I'm grateful to my supervisors in Naples, Rosario De Rosa and Leopoldo Milano, who first introduced me to this field and for always supported me, giving me the possibility to participate in the Summer Student grant, offered by INFN.

I'm indebted to my laboratory group for their contribution to various sections of this thesis: Gong Pu, Andrey V. Rodinov, Vladimir Dergachev, Amanda O Toole, Morgan Asadoor, Abhik Bhawal, Andrea Lottarini, Luca Naticchioni and Arianna Di Cintio.

Thanks to Christian Cepeda and Larry Wallace for their great technical support during the experimental setup and data analysis and a special thanks to Cindy Akutagawa, Marylin Wright and all the LIGO people who helped me during my Californian experience.

I want to deeply thank my family and little Lady who supported me during all this beginning university years and during this period at Caltech. A strong thanks goes to Assunta De Nisi, Assunta Perone and Salvatore Scarpato because without their help and their moral support I'm sure I would not have got my degree.

I thank Carmina Migliozzi, Daniela Finozzi and Teresa Cuomo for their support especially during this last year.

In conclusion, I'm indebted, for lecture notes and help during these university period, to Riccardo Musella (mainly for the long telephone conversations about quantum mechanics), Imma Rea (I will never forget that

August spent studying Mechanics and Thermodynamics together with mosquitos sharing dreams and aspirations), Francesca Emiro (my great laboratory group during these years and a friend of the long " Posposti " courses), Fiammetta Conte, Antonio Bellotta, Enrica Iaccio and Silvia Tuzi (mainly for their strong support during the final examinations period).

Chapter 1

Gravitational Waves

1.1 Gravitational Waves as solutions of Einstein field equations

At the end of the XIX century, the discovery of electromagnetic waves and the connected experiments in this direction gave a real and concrete entity to the electromagnetic field, considered until that time no more than an elegant mathematical trick. It was the collapse of the idea about distance – interactions.

Einstein's *Relativity Principle* and the consequent idea to it connected, according which any interaction among bodies is described by a finite propagation speed, stated the existence of a real and concrete field that acts as the mediator of the interaction. From a philosophical viewpoint this was the new Copernican revolution: physical interest moved from interactions to fields. In this sense the theory of General Relativity (GR) was something like a revolution inside a previous revolution. Following Maxwell's electromagnetic path, the aim of the modern physics was the building of a gravitation – dynamics without significant outcome. Einstein's theory was radically different: gravitational field isn't contained inside space – time, in fact *Gravitational field and Space –Time are the same physical reality*. The drop of heavy bodies is not due to an interaction (neither field interaction nor distance interaction), but to the "natural" movement of free bodies along space – time geodesics. Gravitational field assumed different dignity and role among all the other fields: according to the GR the study of this entity corresponds to the study of the properties of the main structure of the Universe, precisely Space – Time. Einstein's equations, which describe Space – Time evolution, are not linear differential equations and for this reason not so easy to solve. By the way, the possibility to linearize these equations in conditions of weak field led to the possibility of Gravitational Waves (GW). Their weak interaction with matter let them propagating through the Universe almost undisturbed, giving in this way detailed information about their sources and the phenomena in which they are involved (for instance the coalescence of black holes) often not possible to study through electromagnetic contributes.

Chapter 1. Gravitational Waves

The existence of such a wave has been inferred indirectly by studying the binary neutron star system PRS1913+16 [1],[2], which loses energy at the rate predicted by GR. The starting point are the Einstein field equations.

By considering a point A in the Space – Time and fixing a local coordinates set integral with the inertial reference system ("normal coordinates"), the expression of Einstein field equation is:

$$R_{\mu\nu} - \frac{1}{2}g_{\mu\nu}R = \frac{8\pi G}{c^4}T_{\mu\nu} \tag{1.1}$$

where $R_{\mu\nu}$ is the Ricci tensor, $g_{\mu\nu}$ the metric tensor, R the scalar curvature and $T_{\mu\nu}$ the stress – energy tensor. These equations connect the curvature of the Space – Time (ST), given by $g_{\mu\nu}$, with the energy – mass distribution in the Universe, expressed by the tensor $T_{\mu\nu}$. ST metric is:

$$g_{\mu\nu}(x) = \eta_{\mu\nu} + h_{\mu\nu}(x) \tag{1.2}$$

Where $\eta_{\mu\nu} = \begin{pmatrix} 1 & 0 & 0 & 0 \\ 0 & -1 & 0 & 0 \\ 0 & 0 & -1 & 0 \\ 0 & 0 & 0 & -1 \end{pmatrix}$ is the metric in

Minkowski 's space and $h_{\mu\nu}(x) \xrightarrow[x \to x_A]{} 0$.

In the weak field approximation in a region around the point A we have $|h_{\mu\nu}(x)| \ll 1$ and then $h_{\mu\nu}(x)$ can be seen as a perturbation of flat ST, giving in such a way the possibility to linearize Einstein's equations. By solving Einstein's equations for the metric (1.2), fixed a particular set of normal coordinates ("harmonic gauge") in the vacuum space and in the linear approximation, we obtain:

$$\nabla^2 h_{\mu\nu} - \frac{1}{c^2}\frac{\partial^2}{\partial t^2}h_{\mu\nu} = 0 \tag{1.3}$$

whose solution is a monochromatic plane wave travelling at c, precisely GW. Considering a GW propagating along x direction and using the *Transverse Traceless(TT)* gauge it's possible to demonstrate that GW has only two physical freedom degrees, which correspond to the two possible polarization states. In fact, in this gauge, the tensor $h_{\mu\nu}$ is transverse and its trace is 0:

$$h_{\mu\nu} = \begin{pmatrix} 0 & 0 & 0 & 0 \\ 0 & 0 & 0 & 0 \\ 0 & 0 & h_{yy} & h_{yz} \\ 0 & 0 & h_{yz} & -h_{yy} \end{pmatrix}$$

The general solution of (1.3) can be written as a combination of two terms taking into account the "plus" and "cross" polarization states:

$$h_{yy} = h_{\oplus} = \mathcal{R}\left\{ A_{\oplus}\, e^{iw\left(-\frac{x}{c}\right)} \right\}, \ h_{yz} = h_{\otimes} = \mathcal{R}\left\{ A_{\otimes}\, e^{iw\left(-\frac{x}{c}\right)} \right\} \qquad (1.4)$$
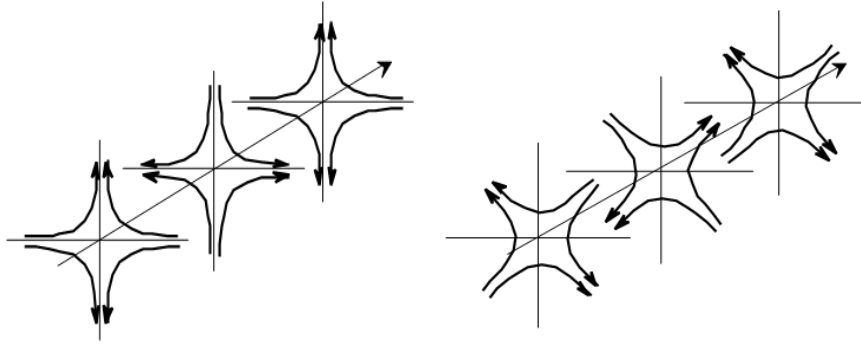

Figure 1.1 GW Lines of force in the two different polarization states for GW:

1.a) $h_{\oplus}$　　　　　　　　　　　　　1.b) $h_{\otimes}$

1.2 GW and free masses

The passage of gravitational waves does not affect the motion of a single particle, because it only changes the metric locally: a free mass has constant spatial coordinates, while surrounding ones are affected by a "*tide force*" described by the tensor $h_{\mu\nu}$. For this reason if we want to detect those waves we have to study the proper distance between two free bodies.

Imbued with linear approximation, we can integrate the equation of *geodesic deviation* of the relative motion of two free bodies of coordinates $x_1 and\ x_2$ obtaining in such a way:

Chapter 1. Gravitational Waves

$$\frac{d^2\xi_i}{dt^2} = \frac{1}{2}\frac{\partial^2 h_{ij}}{\partial t^2}\xi^j \qquad (\xi = x^2 - x^1) \tag{1.5}$$

In the Hypothesis $|\delta\xi(t)| \ll |\xi|$ and that in the observation region (around $x = 0$) be $h_{ij}(x) \approx h_{ij}(t, x = 0)$, we obtain:

$$d\xi_i = \frac{1}{2}h_{ij}(t)\xi^j \qquad where \ h_{ij}(t) \equiv h_{ij}(t, \dot{x} = 0) \tag{1.6}$$

This relation suggest the introduction of the so called *Adimensional Amplitude* h_{yy}:

$$\frac{\Delta l_{AB}}{l_{AB}} = \frac{h_{yy}}{2} \tag{1.7}$$

where $\dfrac{\Delta l_{AB}}{l_{AB}} \ll 1$ is the relative variation of the distance between the two free masses, in way to characterize easily GW intensity, not considering the polarization state. Equation (1.7) points out that the relative distance between two bodies (even of constant spatial coordinates) will extend and contract at the frequency of the GW crossing them.
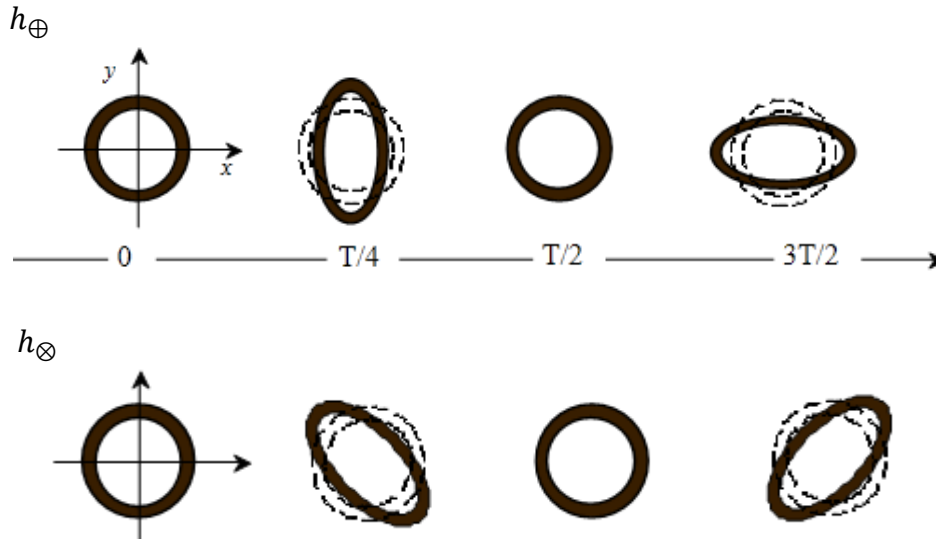
$h_\oplus$

$h_\otimes$

Figure 1.2: Effect produced by a GW crossing a free drop masses ring settled on the plane normal to the wave propagation direction. It's shown the ring deformation for each quarter of period for both the polarization states.

11

1.3 GW Generation

In presence of sources the Einstein linearized equations become:

$$\nabla^2 h_{\mu\nu} - \frac{1}{c^2}\frac{\partial^2}{\partial t^2}h_{\mu\nu} = -\frac{16\pi G}{c^4}\left[T_{\mu\nu}(x) - \frac{1}{2}\eta_{\mu\nu}T^\lambda\lambda(x)\right] \qquad (1.8)$$

where $T_{\mu\nu}$ is the stress – energy tensor of the source. If source dimension and emission waves length are shorter than observer distance r, it's possible to develop the stress – energy tensor in multipoles, as in the electromagnetic case. By the way, on the contrary of the electromagnetic case, gravitational radiation cannot be associated with a dipole contribution. In fact, by defining the gravitational dipole moment $\vec{d} = \sum_i m_i \vec{r_i}$ and by observing that for an isolated masses system the total momentum must be conserved, we understand $\frac{d^2}{dt^2}\vec{d_G} = 0$ and then the first term not null in the multipolar expansion is the quadrupolar one:

$$Q_{\mu\nu}(t) = \int \rho(t,r)(x_\mu x_\nu - \delta_{\mu\nu}\frac{|r|^2}{3})dV \qquad (1.9)$$

This development is very useful to give an estimation of GW amplitude. For the strongest component of the gravitational radiation we obtain:

$$h_{\mu\nu} = \frac{2G}{c^4 r}\ddot{Q}_{\mu\nu} \qquad (1.10)$$

where r is the distance from the emitting source and $\ddot{Q}_{\mu\nu}$ is the second time derivative of the reduced quadrupole moment defined in the (1.9).
Since the term $\frac{G}{c^4}\sim 10^{-50}\frac{s^2}{g\,cm}$ it's clear that GW amplitude is extremely small.
In the not relativistic – approximation the formula for mean emitted power (luminosity) is:

$$\frac{dE}{dt} = \frac{1}{5}\frac{G}{c^5}<\ddot{Q}_{\iota J}\,\ddot{Q}_{\iota J}> \qquad (1.11)$$

For an astrophysics source of mass M and linear dimension R, characterized by motions of period T, approximating $Q \sim \varepsilon M R^2$ where ε is the roundness factor, the (1.11) becomes:

$$\frac{dE}{dt} \approx \frac{G}{c^5}\varepsilon^2\frac{M^2 R^4}{T^6} \qquad (1.12)$$

Introducing the characteristic speed $v = \frac{R}{T}$ and expressing the mass M in term of the Schwarzschild radius $R_S = G \frac{M}{c^2}$ the (1.12) becomes:

$$\frac{dE}{dt} \approx \varepsilon^2 \frac{c^5}{G} \left[\frac{R_S}{R}\right]^2 \left[\frac{v}{c}\right]^6 \qquad (1.13)$$

where the brackets [..] express the spatial average on regions of some wave lengths dimensions.

From the (1.13) it's evident, in the approximation of weak field and small speed, that a <u>useful GW source must be compact ($R \approx R_S$), relativistic (they are characterized by very fast internal movements) and strongly asymmetric.</u>

Now it is clear it is not possible to produce GW of significant intensity in a laboratory. We can only detect them from the astrophysics source we have. Indeed, it is very important having good theoretical conjectures about the GW sources we are using for detection in order to be able to distinguish signals from background noises. This is the most difficult problem because of the complexity of the phenomena involved in GW emission from sources not directly observable from electromagnetic viewpoint. In this sense the most useful are coalescing binary systems.

Astrophysics signals of gravitational origin are usually classified, according their temporal behaviour, in three types :

a) *Impulsive signals*, characterized by a time very small respect to detector observation period (some months);
b) *Periodic signals*, if they are combination of sinusoidal signals of approximately constant frequency on long temporal intervals respect to the observation time ;
c) *Stochastic signals*, if they fluctuate statistically and their characteristic time is large compared to the observation one.

Each type of signal is emitted by a different source. Impulsive signals are emitted by phenomena involving strong gravitational collapses, such as Supernovae generation or coalescence between two massive bodies. Periodic signals are generally produced by binary system (for instance composed by black holes or neutron stars). The most common example for Stochastic signals is the background of the primordial gravitation radiation.

GW trend is important to compare GW Amplitude with detector noise level we are using. This latter is generally expressed in term of linear spectral equivalent density (equivalent *lsd*)[1] defined by the relation:

$$\widetilde{h_n}(f) = 2\tilde{x}_n(f)/L \tag{1.14}$$

where $\tilde{x}_n(f)$ is the 1sd of the test mass displacement.

In case we are considering an impulsive wave of duration τ whose spectrum covers a range $\Delta f \approx \frac{1}{\tau}$, we have the following signal to noise ratio:

$$\frac{S}{N} \approx \frac{h_{rms}}{\tilde{h}_n(\Delta f)} \sqrt{\tau} \tag{1.15}$$

Where $\tilde{h}_n(\Delta f)$ is the equivalent lsd of the noise after we have done an average on the frequencies range $\Delta \nu$ and h_{rms} is the *rms*[1] of the signal.

If we are working with a periodic wave of frequency ν_0 (strict frequencies band), the limit is imposed by the observation time T and the (1.15) becomes:

$$\frac{S}{N} \approx \frac{h_{rms}}{\tilde{h}_n(\Delta f)} \sqrt{T} \tag{1.16}$$

1.4 GW Sources

1.4.1 GW from coalescing binary system

The most important physical event we can consider as GW source is the coalescing of a binary system composed by two massive bodies, such as neutron stars or black holes. The reason of its great utility in this direction is double:

- first of all because of its copiousness. About half of Milky Way stars (probably this is true for all the other galaxies) is part of a binary system

- there is a good precision grade in the theoretical counts in such a way to have detailed predictions about emitted waves and their analysis data.

---

[1] For a signal $x_T(t)$, observed on a temporal interval T with Fourier transform $\widetilde{x_T}(f)$, in literature is generally defined the *power spectral density (psd)*: $S_x(f) = \lim_{T \to \infty} \frac{2}{T} |\widetilde{x_T}(f)|^2$, the *linear spectral density(lsd)* $\widetilde{x_T}(f) = \sqrt{S_x(f)}$ and its quadratic mean value *rms* $x_{rms} = [\int_0^\infty S_x(f) df]^{\frac{1}{2}}$.

If the binary system is composed by two compact bodies such as neutron stars or black holes, the system can emit gravitational energy. At the beginning we have two bodies moving on a circular orbit around their common centre of mass.

During this phase, gravitational emission is not so intense and we can consider periodic emission signal.
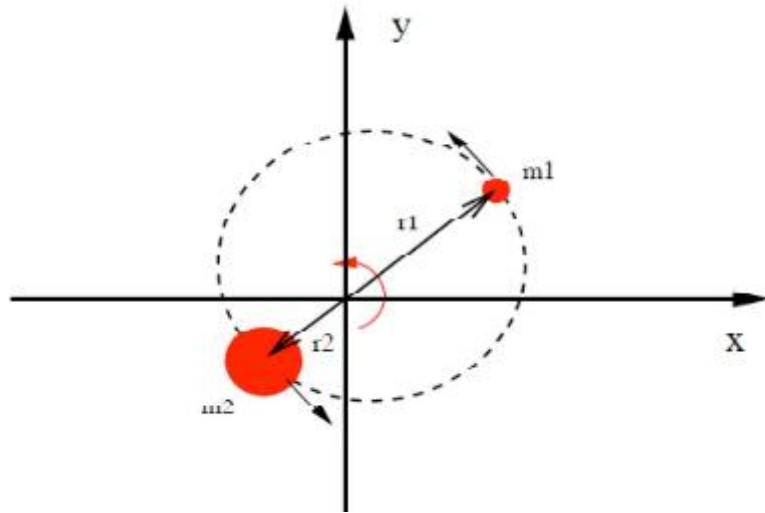

Figure 1.3: Binary system rotating around its centre of mass.

The study of system dynamics is very easy during *Newtonian* phase (till is possible to neglect relativistic effects that will give a huge contribution during the ending coalescing phase because of strong interactions between two gravitational fields). During this phase the system loses energy because of strong gravitational emission and accelerates following a spiral movement, system orbital energy and period decrease: this is the *coalescence phenomena*. The signal emitted during this phase, called *Chirp*, is approximately periodic of increasing amplitude and frequency. The maximum frequency will be:

- $\sim 1\ kHz$ for a binary system made by neutron stars
- $f_{max} \cong \dfrac{10\ kHz}{\frac{M_1}{M_\odot}}$ for a binary system made by two black holes, of

  which the most massive has mass M_1.

In the case of neutron stars, during the periodic phase of orbital movement, gravitational emission is too weak and emission frequency is too small to be detected from Earth (mHz). On the other hand, during the coalescence phase, GW orbital frequency and amplitude will increase, giving to

interferometric antenna the possibility to detect GW during the last binary system life – phase. For instance, if we consider the coalescence of two neutron stars of mass $\sim 1.4\,M_\odot$ ($M_\odot = 1.99 \cdot 10^{30}\,kg$, it is solar mass), we have the following GW dimensionless amplitude:

$$h \cong 8.7 * 10^{-21} \left(\frac{\mu}{M_\odot}\right) \left(\frac{M}{M_\odot}\right)^{\frac{2}{3}} \left(\frac{100pc}{r}\right) \left(\frac{f}{10^{-3}}\right)^{\frac{2}{3}} \tag{1.17}$$

where $M = m_1 + m_2$ is the total mass and $\mu = \frac{m_1 m_2}{M}$ is the reduced mass of the system.
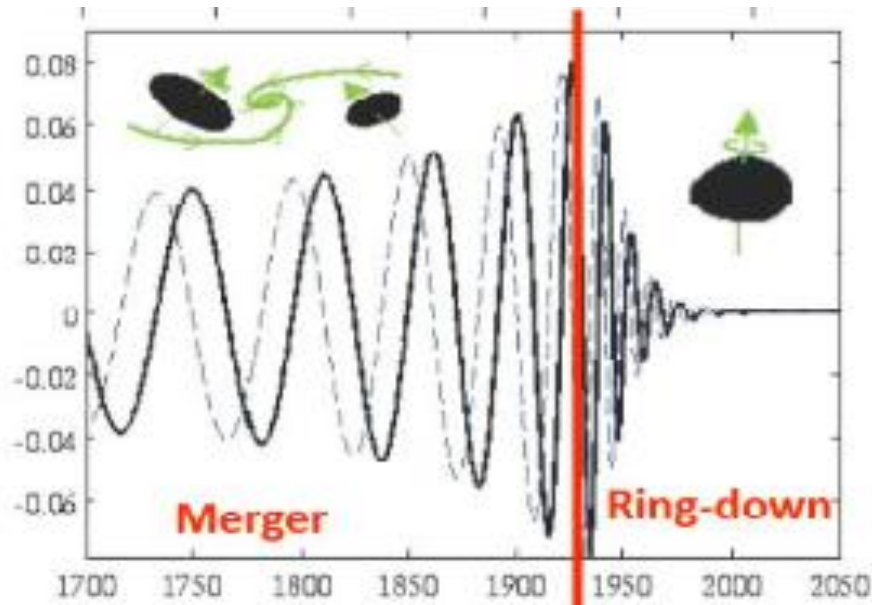

Figure 1.4: Characteristic waveform generated by coalescing bodies.

Moreover considering the time τ spent around the frequency f and defined by the relation $\tau = \frac{df}{dt}\frac{1}{f}$ we have [3] for white noise:

$$\frac{S}{N} \propto f^{\frac{-2}{3}} \tag{1.18}$$

From (1.18) it is evident that a good antenna must be sensible at low frequencies to be an helpful device to detect signals.

While for Electromagnetic waves is not possible to have source position measure from polarization one, in the GW case it is possible. From this viewpoint, one of the application for GW detection is the measure of

distances not possible with the actual devices and in conclusion a good esteem for Hubble constant.

In 1975 R. A. Hulse and J. H. Taylor measured orbital period reduction for the system 1913+16 (composed by two pulsars) obtaining $P \approx -2.4 \cdot 10^{-12}$. Today, after about a long observation period (about 40 years) the value measured is $P \approx -(2.4184 \pm 0.0009) \cdot 10^{-12}$. This result was the first indirect proof about GW existence. Hulse and Taylor won Nobel Prize in the 1993.

1.4.2 GW from Pulsars

Pulsars are neutron stars quickly rotating .They emit periodic electromagnetic impulses and the period of the impulses sequence is equivalent to the star rotating period. Many pulsars emit in the radio range, but there are cases in the visible band (Crab pulsar) and at more high frequencies. Generally pulsars are divided in two types: millisecond pulsar with a period P < 20 ms, old pulsars, and pulsars characterized by greater rotation period, young pulsars.

Pulsars can emit *periodic GW* because of deviation from spherical symmetry in mass distribution. There are two deviation origins:

➢ Solid crust or core can be deformed because of evolution history.

➢ Internal magnetic field, if sufficient strong, could generate a magnetic pressure able to deform locally the star.

Considering elliptical symmetry for pulsar, dimensionless GW amplitude will be:

$$h = 4.2 \cdot 10^{-22} \epsilon \left(\frac{1s}{P}\right)^2 \left(\frac{kpc}{r}\right) \left(\frac{I_3}{10^{38} \, kg \, m^2}\right) \tag{1.19}$$

where $\epsilon = \frac{2(a-b)}{(a+b)}$ is asymmetry factor, a, b are the two axles, I_3 is the inertial moment long rotation axis and P is the rotation period.

1.4.3 GW from Supernovae

Supernovae (SN) are connected with impulsive signals. They are generally divided into two categories:

- o Type I. Their origin is a binary system composed by a white dwarf (WD) and a massive companion. WD increases its mass stealing matter from the star until Chandrasekhar limit (1.44 $M_\odot$). At this point we have a gravitational collapse and consequently core temperature achieves the value necessary for nuclear burnings of massive elements such as C. Energy produced is so high ($\sim 10^{44} J$) to generate a violent deflagration, generally able to destroy the star.

- o Type II. Their origin is the gravitational collapse of a massive evolved star, it is considered the mechanism for the formation of a neutron star.

GW emission from SN takes place during gravitational collapse phase and their intensity depends strictly from collapse asymmetry: a perfectly spherical collapse will not produce GW, a strongly asymmetric collapse will produce a huge amount of GW. According to recent studies type I SN are able to product more intense GW because of centrifugal forces that lead gravitational collapse while WD increases matter in great rotation.
GW produced by SN events would be detected in the frequency band $(10^2 - 10^3)Hz$ and are characterized by a dimensionless amplitude given by:

$$h \cong 2.7 \cdot 10^{-20} \left(\frac{\Delta E_{GW}}{M_\odot c^2}\right)^{\frac{1}{2}} \left(\frac{1kHz}{f_c}\right)^{\frac{1}{2}} \left(\frac{10 \, Mpc}{r_0}\right) \qquad (1.20)$$

where ΔE_{GW} is the GW energy and f_c is the source characteristic frequency. The limit of this model is our not detailed knowledge about gravitational collapse. In other words it is not possible to predict the form of the signal produced from SN. It changes appreciably according to the theoretical model considered.

1.4.4 GW from stochastic background

Actual cosmological models predict the existence of a gravitational radiation stochastic background produced during the first expanding phase of the Universe (about $10^{-44}s$ from Big Bang) and characterized by the following properties: isotropy, stationarity and absence of polarization. This fossil background would preserve information about first Universe and physics connected to it.
Moreover, because of the scanty direction properties of interferometric antennas and because of the huge number of GW sources spread through the

whole Universe, GW overlap giving as result a casual signal. In particular it is expected a stochastic signal originated from about 10^5 pulsars settled in the middle of Milky Way. It is modulated in amplitude with a period of about 24 hours because of Earth rotation.

Chapter 2

Gravitational Waves Detectors

2.1 Interferometric detection technique

In the previous chapter (see par. 1.2) it was shown how GW influence a system of two free masses, in particular way their relative distance (see eq. (1.7)). Since GW amplitude is very small it is expected a very small relative distance variation. The most helpful device to measure a such variation is, without any doubt, a Michelson interferometer because of its large sensitivity respect to length variation of its arms.

A Michelson interferometer is a measurement instrument based on the interference of two coherent light beams. It is composed by a monochromatic light source, a beam splitter (BS) made by a glass plate characterized by an external silver surface, a compensator plate perfectly similar to the BS but without silver external surface and two mirrors placed at distance l_1 and l_2 from BS along normal directions. In literature the optical path length from BS to the terminal mirror is generally called the interferometer arm.
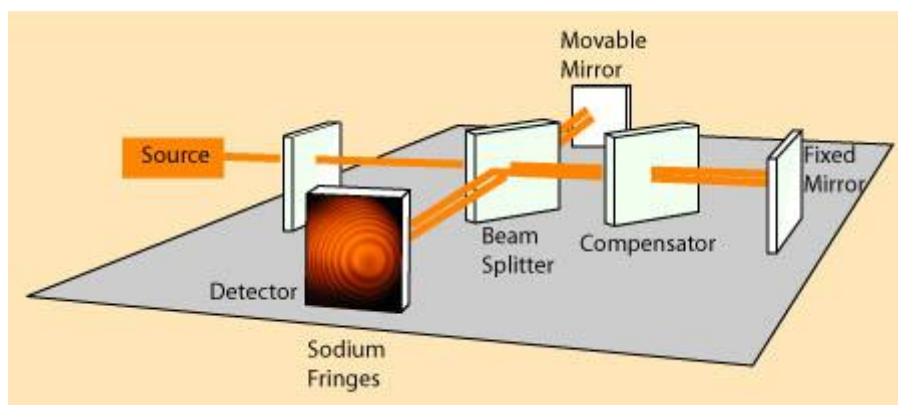

Figure 2.1 Michelson Interferometer scheme.

Chapter 2. Gravitational Waves Detectors

The incoming laser beam is divided by the beam splitter into two equal intensity and orthogonal beams, which move along the arms in such a way to be reflected, at the end of each arm, by a mirror. The two reflected beams will recombine on the beam splitter surface. If the two mirrors are perfectly orthogonal and beam splitter is at the angle of 45° respect to them, the reflected beams, recombining on the BS surface, generate an interference figure. A fraction of the recombined beam is transmitted through the BS and the remaining part is reflected. The intensity of such beam can be detected by a photodetector.

Considering a GW passing through the interferometer, the difference between the travel time of each laser beam into the two arms is:

$$\Delta\tau(t) = h(t)\frac{2L}{c} \tag{2.1}$$

where L is the arm length. It can be helpful to write (2.1) in term of wave phase variation:

$$\Delta\phi(t) = \Delta\tau(t)\frac{2\pi}{T} = h(t)\frac{4\pi}{\lambda}L \tag{2.2}$$

where λ is the laser wavelength. This relation is the GW detection Bible. From (2.2) it is evident that $\Delta\phi(t)$ is proportional to *h(t)* and **L**: for a given value of *h(t)*, GW detection depends on arm's length. To detect GW of amplitude $h \sim 10^{-21}$ passing through a Michelson interferometer of arms length L = 1 km with a laser of wavelength $\lambda = 1\mu m$, it would be necessary to detect a wave phase variation $\Delta\phi(t) = 10^{-11}$ rad. To increase $\Delta\phi(t)$, GW interferometric detectors are designed in such a way to have the arm length L of thousands of km. This is possible in space while it is necessary to find another solution for ground – based detectors. The idea is to insert in each arm a Fabry – Pérot cavity. It consists of two mirrors inserted as shown in the following figure:
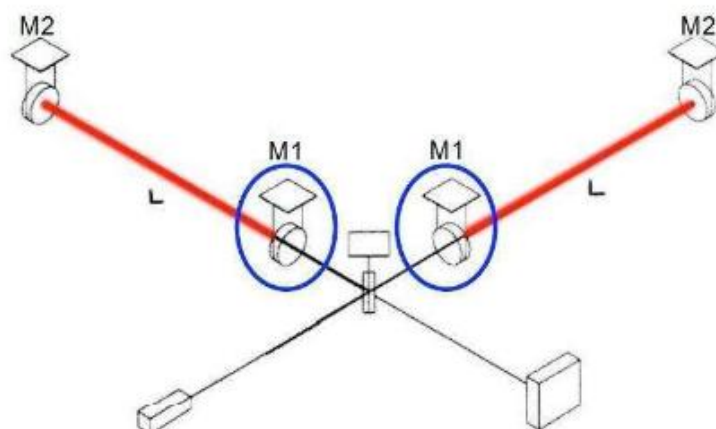
Figure 2.2 Optical scheme of two Fabry – Pérot cavity placed along the two arms of a Michelson interferometer. Each cavity is composed by M_1 and M_2 mirrors. M_1 is the input mirror for each cavity, placed between beam splitter and terminal interferometer mirror M_2.

In such a cavity, the light passing through mirror M_1 is reflected by M_2 covering several times the distance L between the two mirrors, giving a constructive interference figure. As a result, a fraction of the light power contained inside F. P cavity is reflected trough M_1 towards BS direction. On the contrary another fraction is transmitted out from F. P. cavity trough M_2.
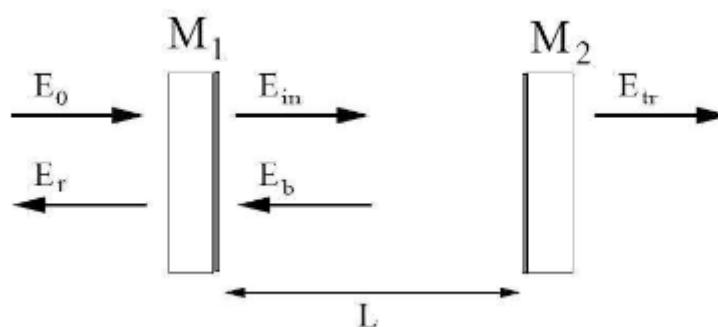

Figure 2.3: Scheme about light radiation inside a Fabry – Pérot cavity. From left: E_0 is incident field on the mirror M_1. E_r is reflected field towards light source, E_{in} is electric field inside cavity, E_b reflected field by M_2, E_{tr} electric field transmitted out from the cavity trough M_2.

Light beam, after passing several times trough F. P. cavity length, L, will have a new phase $\phi = \frac{2\pi L}{\lambda}$. It is possible to demonstrate that the transmitted power is a function of ϕ [4]. When ϕ is 2π whole multiple ($\phi = 2\pi k, k = 0,1,2,\ldots,N$), cavity is in resonance condition and interference between incident light on M_1 and light inside cavity will be constructive. Distance between two consecutive resonances ($k > 1$) is called in literature *free spectral range (FSR)*. It is defined respect to the frequency of light incident on the cavity:

$$\delta f = \frac{c}{2L} \tag{2.3}$$

Or respect to the cavity length:

$$\delta f = \frac{\lambda}{2} \tag{2.4}$$

The ratio between *FSR* and Cavity Resonance amplitude at half height, *FWHM*, is called *FINESSE*:

$$F = \frac{FSR}{FWHM} \tag{2.5}$$

Light phase difference in the two arms of a simple Michelson interferometer is given by $\phi \propto \frac{4\pi}{\lambda}\Delta L$, while in the case of an interferometer with F. P. cavity, we have $\phi \propto \frac{4\pi}{\lambda}\Delta L \frac{2}{\pi}F$, because of in a such interferometer, arms optical path difference is multiplied for $\frac{2}{\pi}F$. Consequently instrument sensitivity will increase of a factor $\frac{2}{\pi}F$.

A photon which enters inside cavity will have $\frac{2}{\pi}F$ reflections before leaving it. Light will spend a time t_s , called *Cavity Containment time,* to cover this path:

$$t_s = \frac{L_{eff}}{c} = \frac{2}{\pi}F\frac{L}{c} \tag{2.6}$$

where $L_{eff} = \frac{2}{\pi}L \cdot F$ is the effective length of the Interferometer.

Each Interferometer, because of its instrumental nature, suffer the influence of several noises that limit its sensitivity. The most important noises for a GW Interferometer are generally classified in three different types:

- Thermal noise: sensor intrinsic noise
- Shot noise, a noise connected with the reading of the signal

- Environmental noise, such as Newtonian noise or Seismic noise

Generally the presence of noise inside an Interferometer will be evident macroscopically by mirrors position variation, effective or apparent. In other words noise introduces an output signal of the instrument very similar to that produced by the passing of a Gravitational Wave. It is necessary to compare oscillation amplitude generated by the noise source with oscillation amplitude generated by GW passing. For this reason we introduce the *Equivalent spectral linear density*:

$$\check{h}_r(f) = \frac{\check{x}}{L} \tag{2.7}$$

where $\check{x}(f)$ is the linear spectral density of a position noise according to the definition given in Chapter 1 (see note at page 6).

Seismic noise

Seismic noise is produced by ground vibrations around Interferometer building site. Ground motion is caused by many factors: human activity (controllable), micro − earthquakes, ocean wave activity, atmospheric pressure variation and movement of the Earth's crust (not controllable). This kind of vibrations are able to influence mirrors positions thanks to mechanical connection between mirror and ground. To attenuate this noise, mirrors must be isolated and suspended by filters. Seismic noise is the dominant limit for the sensitivity of the Interferometer in the low frequencies band (f < 10 Hz). In this direction moves my personal contribute, as it will be developed in the following chapters. Unfortunately we don't have an universal law to describe seismic noise: its intensity can change, even for different order of magnitude, according to the observation place and day, because of its dependence from human activity around Interferometer building site. In this sense it is possible a notable variation even between night and day. The general seismic noise spectral density is described by:

$$x(f) = \frac{\delta}{f^2} \frac{m}{\sqrt{Hz}} \tag{2.8}$$

where the δ constant changes with respect to the site between 10^{-9} and 10^{-6}. At 10 Hz, a value of $\delta \sim 10^{-6}$ would thus produce a displacement, in the test masses position, of $10^{-8} \frac{m}{\sqrt{Hz}}$, which is several orders of magnitude greater than the GW amplitude we want to reveal. Seismic isolation is thus the more difficult problem to solve at low frequencies.

Let us consider a seismic isolation system for the Interferometer mirrors realized by suspending tests mass of the mirrors. Calling x_0 the masses equilibrium point and $k = \frac{mg}{l}$ the elastic constant of suspension pendulum, neglecting dissipation term and without external forces, _Mirror dynamics equation_ gives:

$$m\ddot{x} + k(x - x_0) = 0 \tag{2.9}$$

By considering a fluctuation from the equilibrium point, due to the seismic noise, Transfer function connected with the equation (2.8) is:

$$\frac{x(\omega)}{x_0(\omega)} = \frac{\omega_0^2}{\omega_0^2 - \omega^2} \tag{2.10}$$

where $\omega_0 = 2\pi\sqrt{\frac{k}{m}}$ is the resonance of the suspension system, and for frequencies $\omega \gg \omega_0$ vibrations are attenuated according to the following equation:

$$\frac{x(\omega)}{x_0(\omega)} \approx \frac{\omega_0}{\omega^2} \tag{2.11}$$

By introducing a system of cascaded oscillators, for instance N, the transfer function will become:

$$\frac{x(\omega)}{x_0(\omega)} \approx \prod_{i=1}^{N} \frac{\omega_i^2}{\omega_i^2 - \omega^2} \tag{2.12}$$

where ω_i are the N resonance frequency. In the condition $\omega \gg \omega_i \; \forall i$, attenuation is given by:

$$\frac{x(\omega)}{x_0(\omega)} \approx \prod_{i=1}^{N} \frac{\omega_i^2}{\omega^{2N}} \tag{2.13}$$

From (2.12) it is possible to understand that, realizing a chain of cascaded oscillators, we can build a low – pass filter in such a way to attenuate mirrors vibrations. Take – off frequency of the chain depends on resonance frequency of the system. Clearly, the goal is to reduce this frequencies, in such a way to have a more large frequencies band in which vibrations are attenuated.

Other Noise Sources

 Newtonian noise is caused by the fluctuations of the masses distribution around Interferometer mirrors. These fluctuations generate a variation of the local gravitational field which consequently will generate a variation of the Interferometer mirrors. This variation can't be reduced by the seismic isolation system already described since it act directly on the test masses. Newtonian noise gives the lower limit of the detection band characteristic of the Interferometer : for $f < 4\ Hz$, the equivalent spectral density is $\widetilde{h_N} >$ $10^{-19}\sqrt{Hz}^{-1}$.

Thermal noise is caused by the fluctuations of a body position which is in thermodynamic equilibrium with surrounding environment, because of its Temperature. It is notable in the systems which use oscillated systems and then our cascaded filters system.

Shot noise is connected with light particle nature.

2.2 VIRGO and LIGO

In the last ten years many interferometric detectors have already been built around the world, such as LIGO (USA), VIRGO (Italy), GEO600 (Germany) and TAMA (Japan) and AIGO(Australia), the youngest brother of the family, still in building phase.

Figure 2.4: Interferometric detectors in the world

Funded by the NSF (National Science Foundation), LIGO [5] is a collaboration between scientists from the Californian Institute of Technology (Caltech) and Massachusetts Institute of Technology (MIT). LIGO operates two GW observatories in unison: The *LIGO Livingstone Observatory* in Louisiana and *The LIGO Hanford Observatory*, located near Washington. The first one consists of two interferometers characterized by arm's length of 4 km and 2 km respectively, and the other one in Livingstone consists of one Interferometer made by 4 km long arms.

Figure 2.5: Livingston and Hanford LIGO interferometers.

To reject environmental and instrumental noises and to determine the direction of the GW sources, two detectors located at widely separated sites

are helpful. Exactly these sites are separated by 3,002 km (1,865 miles). Since GW are expected to travel at the speed of light, this distance corresponds to a difference in GW arrival times of up to ten milliseconds. Through the use of triangulation, the difference in arrival times can determine the source of the wave in the sky. LIGO applies two modifications to the simple Michelson interferometer: each arm contains a resonant F. P. cavity to increase instrument sensitivity. A partially – reflecting mirror is placed between the laser and the BS to implement power recycling. As a result LIGO interferometer increase the power in the arms by a factor of 8,000 with respect to a simple Michelson interferometer. The laser source emits a beam with a power up to 35 Watts in a single frequency at 1064 nm that passes through an optical mode cleaner before reaching BS at the vertex of the Interferometer. The optical mode cleaner has the function to stabilize light source. All the optical components are placed in a ultra - high vacuum system to suppress, as much as possible, air noise and to have a good acoustic isolation. Since the most important source of noise in the low frequencies region is given by seismic noise, it is necessary a system to minimize it. It is possible to realize this condition by suspending all the mirrors by a system of four pendulums (see Chapter 3). The position and orientation of the suspended optics is controlled by electromagnetic actuators.

The *LIGO(Laser Interferometer Gravitational Wave Observatory) Livingstone Observatory* was successfully upgraded in 2004 with an active vibration isolation system based on hydraulic actuators providing an isolation factor of about 10 in the 0.1 – 5 Hz band. Seismic vibration in this band is mainly due to micro seismic waves and anthropogenic sources such as traffic etc... On the contrary, the *LIGO Hanford Observatory* has been able to preserve its primordial original passive seismic isolation system because of limited geologic activity in the Southeaster Washington.

VIRGO [6] is an European project, funded by the French CNRS and the Italian INFN, located within the site of EGO (European Gravitational Observatory), based at Cascina, near Pisa (Italy). VIRGO takes its name from galaxies clump in which it would investigate to detect GW. It is very similar, from an optical viewpoint, to his USA companion LIGO. Its arms are 3 kilometres long. To achieve a better sensitivity, in each arm is inserted a F.P. cavity in such a way to increase the optical length from 3 to about 100 kilometres. Moreover, to increase the beam power, a recycling mirror is placed just after the interferometer input, exactly as in LIGO.

Figure 2.6: VIRGO observatory and its Interferometer

VIRGO's most characteristic is that each optical element is suspended to a seismic isolation system contained in a vacuum tower. In fact seismic noise is the dominant form of noise in region of low frequencies in the revelation band of a GW interferometric detector. To solve this kind of problem, VIRGO uses a particular system called *Super Attenuator* composed by three parts:

- Pre – Isolator
- A chain of five seismic passive filters
- Payload

Super Attenuator is essentially made by a chain of five pendulums (passive filters) able to oscillate and to attenuate seismic vibrations at a frequency higher than the resonance frequency of the system. In other words it is a low pass – filter for ground vibration characterized by a cut-off frequency $f_0 < 1$ Hz. Each filter is connected in sequence at the following by a steel wire. The last filter, generally called "Filter 7" because the original project consisted of 7 filters and not only 5, supports through a cross – structure called "Marionetta", the optical component. The whole wire, from the suspension point to the mirror, is 10 meters long. By the way, to attenuate vertical ground vibrations, that influence mirrors horizontal position, each filter is helped by a system of triangular cantilever Maraging blade springs, very similar to that used in LIGO and that will have great importance in this whole thesis work. Finally, to have a better response at low frequencies, the components described above are mounted on an elastic structure that has the function of an *Inverted Pendulum (IP)*. It consists of three aluminium poles, 6 m long, fixed at the basis by steel joints which give the system the necessary elasticity. Resonance frequency of IP is given by:

$$f_0 \quad = \frac{1}{2\pi}\sqrt{\frac{k}{M} - \frac{g}{l}} \qquad (2.14)$$

where M is loading mass of the system (supposing negligible the masses of IP), k is the elastic constant of the joints and l is the length of every pole. Operating a wise choice for each of this parameters it is possible to have $f_0 \approx 30 \, mHz$, corresponding to a normal pendulum 280 m long. Consequently this represents a good Pre – Isolation stage for low frequencies.
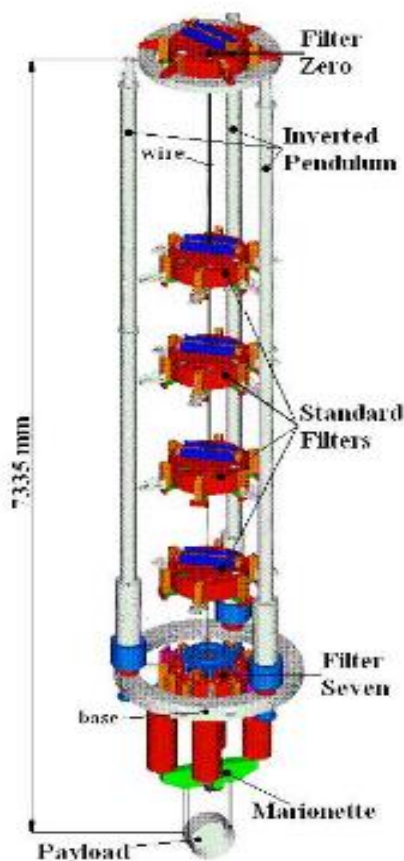

Figure 2.7: VIRGO Super Attenuator

VIRGO uses two F.P. cavity inside the two arms (L = 3 Km) with F = 50 and consequently $L_{eff} \sim 95$ Km. When the Interferometer works in destructive interference, most of input laser power is reflected back towards laser source and consequently it will be lost. A fraction of this power can be reutilized putting a partially transmitting mirror between the laser source and BS: this is the so called power recycling.

Early GEO600 joined within the LIGO project and later, in 2007, VIRGO and LIGO started a very strong common observation. They still work as an unified

system. First generation LIGO was projected to be GW sensitive in the frequency band 40 – 7000 Hz, while VIRGO is sensitive in a wider frequency range, from 10 to 10000 Hz. This frequency band should give us the possibility to detect GW caused by the coalescence of binary system or produced by pulsar and supernovae in the Milky Way and nearby galaxies, but, up to now, no signal was detected.

2.3 Future GW Detectors

The description given above is about *First Generation GW Detectors*. In the last years a new and more sensitive generation (we shall gain more than a factor of 10 in sensitivity in the same frequency range) is birthing: *Advanced LIGO, Advanced VIRGO* and *LISA(Laser Interferometric Space Antenna)*, the first space – based GW observatory whose goal is GW detection in the range $10^{-4} - 0.1\ Hz$.
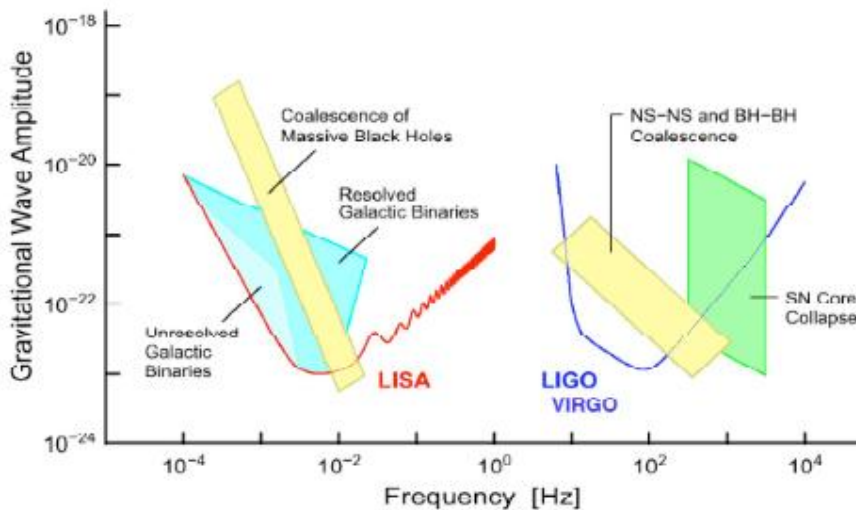

Figure 2.8: The sensitivity curve of Advanced detectors and LISA

Even considering LISA help, the frequency band 0.1 – 10 Hz, the most interesting, will be not covered. LISA sensitivity is limited, at high frequencies, by the laser shot noise, while the sensitivity curves of VIRGO and LIGO are limited, at low frequencies, by the seismic and Newtonian noise, which represents the dominating noise source below 10 Hz. However LIGO is able to reach a good sensitivity ($S_n^{\frac{1}{2}}(f) \leq 10^{-19} Hz^{\frac{-1}{2}}$) only above 40 Hz and Advanced LIGO above 10 Hz; below these frequencies. Below these frequencies there is the so called "seismic wall", which depends from the resonant frequency of the used attenuator.

Chapter 2. Gravitational Waves Detectors

The goal and motivation for the next generation, the third one, of GW detectors is the improvement of the low frequencies behaviour and the exploration of the 0.1 – 10 Hz band. There are different idea and one of the most interest is the DUSEL (Deep Underground Science and Engineering Laboratory)[7] proposal. Funded by Caltech, the University of Minnesota, Florida, Carleton and Louisiana State, its goal is to achieve the frequencies band 0.1 – 10 Hz going underground. Since 2008 there is a group acquiring a detailed set of seismic motion measurements in the Homestake mine, South Dakota. Their final goal is a model to estimate the Newtonian noise caused by the measured seismic noise. Why the idea is going underground? There are many types of seismic waves able to produce fluctuations of the local gravitational field, but Rayleigh waves, which have both vertical and longitudinal components, are the dominant ones from this viewpoint. This kind of wave are characterized by an interesting property: the displacement decreases exponentially with depth. Developing a GW detectors could be helpful for many reasons: the exponential reduction of seismic noise, which is proportional to $e^{\frac{-4d}{\lambda}}$ where d is the depth and λ the wavelength . Considering that the speed of sound 2 km underground is around 5 km/s, we understand that seismic waves in the 0.1 – 10 Hz band will have a very large wavelength, around 500 m – 50 km. A such a value is much larger than the size of a cavity that should contain the Interferometer mirror. Consequently seismic wave passing through this cavity, will be able to change weakly only the gravitational field at the centre of the cavity. Moreover atmospheric fluctuations should have negligible effects on the gravitational field deep underground. In addition to this, human activity influencing gravitational fluctuations are much more controllable. Nevertheless there are still "black holes" in our knowledge about the underground interferometer behaviours like the possibility to predict the functional dependence of seismic noise amplitude on depth and frequency or geological problem such as the non uniformity of underground rock density and how it could influence the gravitational field fluctuation.

A similar project, in designing phase, is *ET (Einstein Telescope)*, a collaboration between ESA and NASA, which motivation is the exploration of the 1 Hz frequency region.

So far, the underground solution seems to be the most promising one for GW interferometric detectors of third generation, apart from the possibility to substitute the Maraging steel blades of the Seismic Attenuator with a new material (this thesis work concentrates on the Glassy one) characterized by a lower dissipation factor as I'll develop in the following chapter.

Chapter 3

Maraging and Glassy blades

3.1 Introduction and goal of the work

One of the major difficulties in GW detection in the low frequencies range is represented by the seismic noise. It is necessary to develop a high performance seismic isolation system. Actually all the GW detectors make use of a seismic isolation system (TAMA, LIGO, VIRGO etc..) based on Maraging steel blades. This material is characterized by a very satisfying attenuation performance at high frequencies, $f > 1\,Hz$, but at low frequencies its efficiency is tried out, as recent studies ([8],[9]) have already revealed. Since all the observed anomalies (such as unusual appearance of the term 1/f in the transfer function [10], hysteretic properties of the materials, the apparent random walk of VIRGO and TAMA IP equilibrium point etc…) are connected with dissipation properties of the material used in blades construction, it is interesting to investigate different materials that may have lower dissipation properties than Maraging for better seismic isolation performance at lower frequencies. In this work the dissipation properties have been studied using Geometric Anti Spring (GAS) filters, which, coupled with an Electro Magnetic Anti Spring (EMAS) mechanism, allow us to explore resonant frequencies below 100 mHz. According to a vast literature from 1950's to 1960's [11] dislocations inside materials are responsible of the internal friction of metals. To be detailed according to another work [12], all the anomalies measured and observed are compatible with a collective movement of dislocations, described by a complex statistical model, known as Self Organized Criticality (SOC). It is well known that dislocations carry stress and contribute to elasticity. At low frequencies ($f < 200\ mHz$) all the anomalies observed result compatible with dislocation disentanglement, yielding a strange dissipation mechanism, hysteresis, thus reducing material elasticity. I have focused on a new material, *LM001 Zr − based bulk metallic glass* (that from now I'm going to name simply *Glassy*, but commercially known as LM001), which don't contain dislocations and then it is expected a lower hysteresis dissipation process with respect to that involved in Maraging materials.

This chapter and the following are the result of my 10 weeks experience at *Caltech(California Institute of Technology)* during summer 2009. In this chapter I will give a quick overview about the materials I have used, the theoretical models explaining dislocations contribute to material elasticity and the mechanical filter used.

3.2 Why Maraging? Why Glassy metal?

As explained in the chapter 2 (par. 2.2) every GW detector makes use of a system constituted by triangular cantilever Maraging blade springs (both SAS and Super Attenuator, SA) to provide for a good vertical seismic isolation. Why Maraging was chosen among the other materials? Maraging steels are iron alloys, known for their strength and toughness without losing in malleability. These steels are a special class of low – carbon ultra – high strength steels. Their strength comes not from carbon, but from precipitation of inter –metallic compounds. The main alloying element is nickel (from 15 to 25%). Moreover cobalt, molybdenum and titanium are added to produce inter – metallic precipitates. The result is a very hard form of crystalline structure known as Martensite interspersed with billions of precipitates, which impede long range dislocation motion. The name Maraging is a portmanteau of Martensite and aging: in fact this steel is aged around 450 °C to generate the precipitates that give it the properties discussed above. Thanks to the low percent of the carbon, Maraging steels have good machinability. Prior to aging, they may also be cold rolled up to 80 – 90% without cracking. They offer good weldability, but must be re – aged afterward welding to restore the properties of heat affected zone. To be precise the Maraging used in the GAS filter is *Maraging Marval – 18* precipitation hardened at 435° C for 100 hours. The blades inside our GAS Filters are subjected to an internal stress of about 900 N/mm^2, which is about 70% of its tensile strength. Many studies report, at room temperature, a gradual lowering of the payload (of μm/day). This phenomena, best known as *microcreep* (or simply *creep*), is originated inside crystals and it is caused from the heavy load acting on the blades. This process introduces a mechanical noise due to the slippage of grain structure of polycrystalline steel, which is able to degrade the sensitivity of the GW Interferometer. A research study [3] compels creep tests on two different GAS filter: one made with AISI 1070 steel blades and one made with Maraging steel blades. In particular way the work shows the temperature dependence of creep in both the cases. In the AISI 1070 GAS filter the creep observed is linear, while the temperature dependence of the creep speed is exponential. The Maraging prototype has been tested at temperatures lower than 80 °C (35 °C, 50 °C) under an applied stress of 900 N/mm^2 held constant for some weeks. The result is strongly different from AISI 1070 one: the Maraging shows a logarithmic creep speed with the residual motion decreasing as 1/t. The creep

was independent from the temperature and the residual creep in those tests is only of about 4 μm/day. Moreover, raising the test temperature up to 80 °C first and up to 65 °C later, the lowering effect of the blade is negligible and consequently the mechanical noise connected to it. In the Maraging steel, increasing of the temperature under applied stress accelerates the depletion of dislocations flow and then the creep effectively stops at lower temperatures. As a result, the treatment of Maraging steel blades under applied stress at 80 ° C, will give us a residual creep lower than 10^{-4} μm/day at the working temperature of the SA, thus it is possible to neglect the creep effect. Now it is clearly explained the choice of the Maraging steel. The effect of dislocation is of fundamental importance and not only for the creep phenomena, but even for the dissipation properties inside the materials, which is a completely separated process, as it will be developed in the following paragraph.

The LM001 is a material of recent development [13]. The X – ray diffraction results show that it is a monolithic bulk – metallic glass (BMG) composed by Zr (41,2 %), Ti (13,8%), Cu (12.5%), Ni (10%) and Be (22,5%) and for this reason called *LM001 Zr – based bulk metallic glass* (LM001). This material has attracted much interest for scientific research and engineering application because of its unusual properties, such as great strengths, high hardness, low friction coefficient, good wear resistances and almost perfect as cast surface. Moreover glassy materials (metals or ceramics), as in LM001 case, don't contain dislocations and then are a very interesting material for both creep and dissipation processes inside the material. Of course, it is necessary a comprehensive study to explore other loss mechanisms involved in their structure that could spoil their performance.

3.3 Inside materials: theoretical model.

In the past the best candidate in explaining materials dissipation properties was viscosity or loss angle. At high frequencies it agrees perfectly with experimental data. The problem comes out at low frequencies because, being viscosity proportional to speed, it is expected that its effects vanish in the zero frequency limit. Low frequencies experiments [9] revealed frequency independent losses and static hysteresis, it was clear that viscosity was insufficient to explain the observed losses. What is then generating the observed losses? In a perfect crystal all the atoms occupy their own positions in the lattice. This model is an idealized one, in fact such a crystal could exist probably only at a temperature T = 0 K. Real crystals, even the most perfect ones, contain a large number of imperfections. A trivial imperfections classifications divides defects in: point defects, line defects, surface defects and bulk defects. Linear defects are generally known as *Dislocation*. They are row of atoms, which don't present the right coordination number. They are generated by a mechanical stress which is able to move two crystal

planes. They are divided into: edge dislocations and screw dislocations. Real crystal contain generally thousands of km per cm^3 of both. To have an idea about their formation we can consider the formation of an edge dislocation through work hardening:

a) Let's consider the section of a cubic crystal in which top and lower surface are subjected to two opposite stress τ. MN line indicates the possible trail of a slip plane.
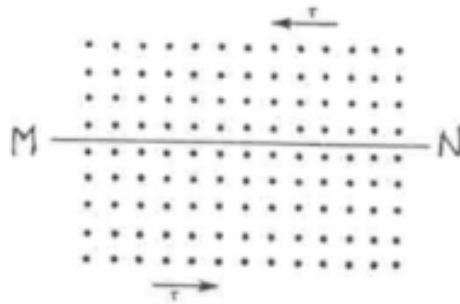
b) Suppose that thanks to the applied stress, the top surface will move of an interatomic position towards left.
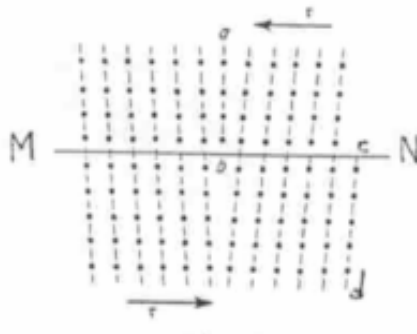
In the previous figure you can see two half planes, *ab* and *cd*, that are vertical respect to the slip plane direction *MN*. The dislocation line *ab* moves like a wave moves on a carpet. Macroscopically the crystal lattice will be deformed and the effect will be clearly evident if the stress applied, τ, is able to move of an interatomic distance the whole crystal lattice as it is shown in the following picture in 3D:
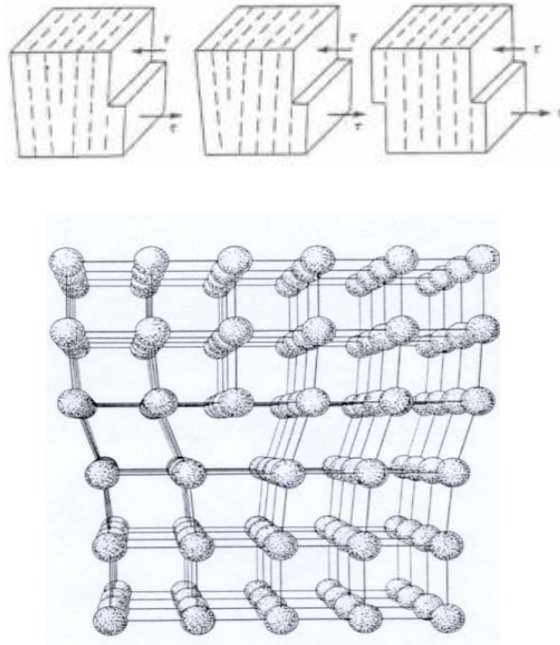
Figure 3.1: Edge dislocation as it appears in a crystal lattice.

The description given for the edge dislocation is perfectly similar to that about the screw ones. The only difference is about the formation way of a screw dislocation:
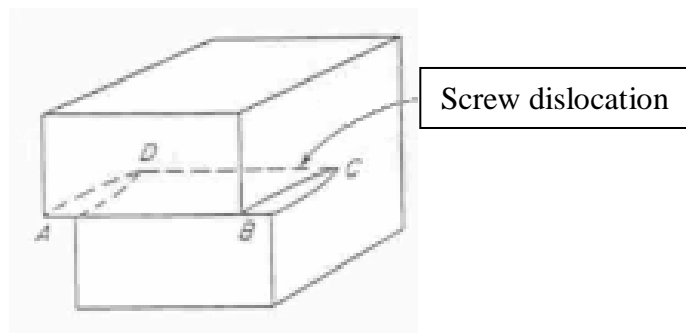

Screw dislocation

Figure 3.2: Screw dislocation

In this case the upper front of the crystal is moved of one interatomic distance from the bottom one in the left direction. The line CD in the figure 3.2 is the screw dislocation line. Let's image to divide the crystal in little cubes each one representing one atom of the crystal, as in the following figure:

Screw dislocation
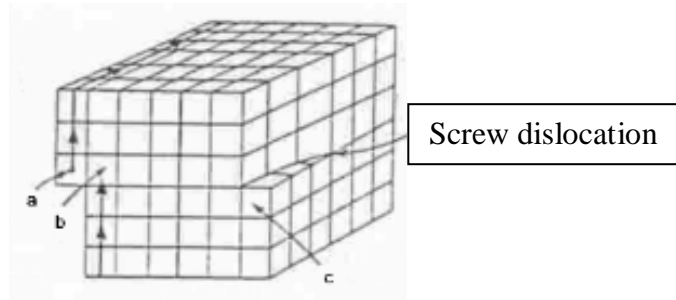
If we start our path from the atom *a* following the direction indicated by the arrows, it is possible to understand that the first spiral is completed in the position of the atom *b*, while the last one is completed in the position of the atom *c*. The model is now clear: the network planes wrap the dislocation in spiral way, like inside a screw: hence the name *Screw dislocation*.

Note that dislocations can either extend from crystal edge to crystal edge, or form loops. No dislocation can end half way.

Also once formed, which require considerable amounts of energy, can move almost freely, thus inducing plasticity, unless impeded in their motion by impurities, precipitates or other dislocations.

In literature is generally described the dislocations movement in term of the *Burgers vector*. Let's consider the section of a perfect (ideal) crystal and one containing an edge dislocation:

Beginning
point   Ending point
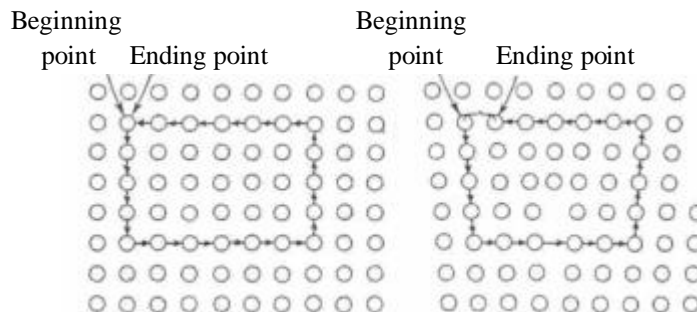
Beginning
point   Ending point

Figure 3.3: Comparative study between

Perfect crystal   Real crystal

In both the scheme is represented a counterclockwise circuit. While in the perfect case the beginning point of the circuit coincides with the ending one, in the real crystal they are different. The vector $\vec{b}$ connecting the beginning and ending point is known as *Burgers vector* of the dislocation. According to this definition, the edge dislocation is orthogonal to $\vec{b}$ and it moves in the direction of $\vec{b}$. The length of $\vec{b}$ is usually equal to the distance between two planes of the lattice (*unit length*). By the way there are crystals containing $\vec{b}$ of lengths bigger than unitary length, but they are unstable and they tend to

split in two unit dislocations. On the contrary, for a screw dislocation is different:

Beginning point

$\vec{b}$

Ending point
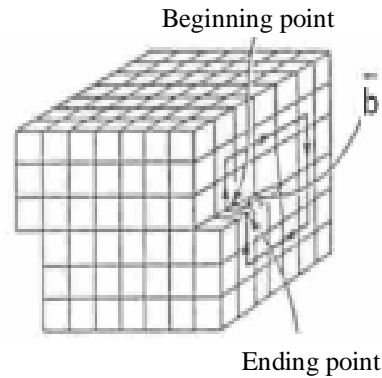
A screw dislocation is parallel to its $\vec{b}$ and it can move in the direction orthogonal to that of $\vec{b}$.

In materials science is commonly accepted that mobile dislocations constitute an important dissipation source in metals. According to the general idea dissipation is due to the incoherent sum of individual dislocations. Collective motion of dislocations provides the most convincing interpretation of materials dissipation properties [12]. In special way the possibility to control dislocation movement gives a huge number of application. For instance in metallurgy, in hardening processes, dislocations are created in such large number that they entangle up to their motion is blocked and the corresponding dissipation is quite completely suppressed (physically the material acquires an higher Q-factor and larger elasticity modulus). Applying repeated plastic deformation we increase dislocation density. Intuitively it is expected that the increasing of dislocations number should be responsible of a major plastic properties of the materials since there is a great number of dislocations able to move inside the material. Unexpectedly it is noticed an improvement of the resistance to further dislocations motions. Why? If dislocation density growths up, dislocations entangle and their movement is impeded. In the presence of low amplitude harmonic stresses, dislocations segments remain pinned inside the crystal and vibrate like ideal elastic strings [9]. As they pile up they get trapped: a trapped dislocation needs to wait for neighboring one to unpin before it can move again. You can image this model thinking to what generally happens Monday morning on the motorway: each dislocation is like a car inside the traffic jam. It is a domino effect: each car must wait that the neighboring one moves before it goes out from jam. This dislocations growth is sometimes called "dislocations wood" because each one has to pass through the wood generated by the others to be

able to move from its initial position. Consequently it will be necessary a more high applied stress to obtain a plastic deformation of the material (cold working). It is shown in the figure 3.2.

Figure 3.2: "Dislocations wood": each dislocation has to pass through the wood generated by the others to move from its initial position. The result is the formation of a domino effect, like traffic jam.

In a precipitated hardened alloy, that is the case of our Maraging blades, as well as in most polycrystalline metals, dislocations can entangle but their number is not enough, as in the case of hardening process, and then they can disentangle under changing stresses. In this case dislocations movement is inhibited by the presence of intermetallic precipitates, essentially finite size point defects (their typical spatial range is about 10^{-9} m). In this model dislocations start their movements up to the point which hosts an impurity, then dislocations pin to the impurity (precipitates and other defects), but also to another one. Interactions can build up but they could be not linear. Again,

as they pile up they get trapped and the model is the same already described above.
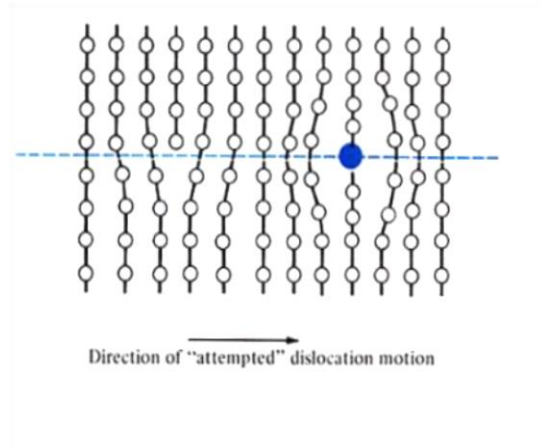

Direction of "attempted" dislocation motion

Figure 3.3: Dislocation line pins to the impurity

Once dislocations movement starts it can engender the domino effect spreading out from the beginning point through huge volumes. Vibrations of pinned dislocation segment are extremely short, on the contrary the domino effect involving a significant number of dislocations needs longer time scale. The description of the relaxation dynamics of a dislocation network is necessarily of a statistical type. The roadmap – model in this case is the so called *Self – Organized Criticality (SOC)* due to Per Bak, Curt and Chao Tang [14]. This model address to complex systems composed by a huge number of elements interacting each other on a small space scale. Many composite systems evolve spontaneously towards a critical state, in which each event, even small, is able to produce a domino effect involving a huge number of system elements. According to this viewpoint, the mechanism which leads to the small events is the same leading to the big ones, even catastrophic. Moreover composite systems don't achieve the equilibrium configuration but they evolve moving from a metastable state to another one. The most simple image to acquire this theory is the formation of a pile of sand. How can we generate a pile of sand? We start putting down a sand grain and later, grain after grain, we generate a pile. The grains overlap according to a conical bulk, characterized by a steep slope. If the slope is excessively steep, the grains engender a little avalanche, leading a part of the grains at the basis of the conical bulk. When the slope achieves a value by which the amount of added grains is equivalent to that lost by avalanches, the system is in "critical" configuration and the pile ends its growth. The system is *self – organized* because it achieve this configuration by itself, without an

external action. Moreover the achieved state is *critical* because the grains added are just stable: a little variation, even only added or subtracted grain, changes the previous configuration. An avalanche represents a domino effect: one instable grain falls down meeting on its falling other grains; if they are also unstable, they fall down together with it, generating the avalanche. The pile of sand is a dissipative system: it is an open system in which every added grain will contribute to the total energy by its own potential energy. When a grain of this is involving in the formation of an avalanche, its own potential energy becomes kinetic one which will be dissipated at the end of the avalanche as heat by friction.

When the pile achieves the critical state, the avalanches number N along a dimension s follows the "*exponentiation law*":

$$N(s) \propto s^{-\tau} \tag{3.1}$$

Taking the logarithm to both members we obtain:

$$log\ N(s) \propto -\tau\ log \tag{3.2}$$

Plotting in a log – log plane we have a straight line of plot $-\tau$. In the case of the pile of sand we have $-\tau = 1.1$.
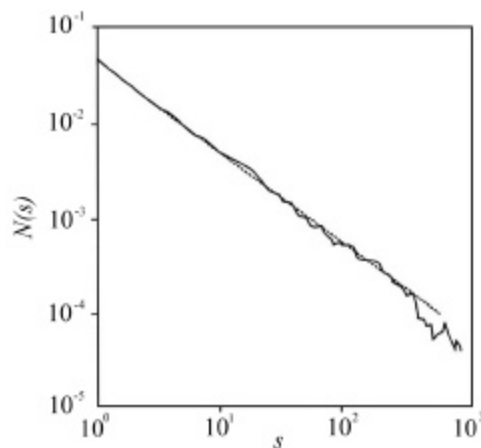

Figure 3.4: "Exponentiation law" for the number of

Avalanches. Legend:

------- theoretical trend, ——— experimental trend.

Moreover, plotting avalanches dimension vs time, it is possible to obtain a signal very irregular called *Flicker*, as shown in the following figure

(to be precise, it is plotted a relative dimension s and not absolute, $\frac{s}{s_{max}}$, where s_{max} is the dimension of the biggest avalanche happened):
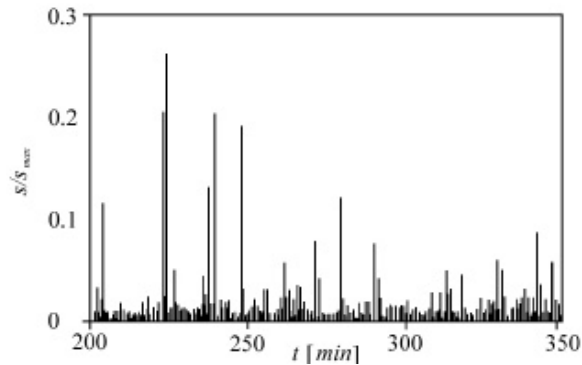

Figure 3.5: Avalanches trend in a pile of sand for a period of 350 minutes.

When a system in the critical state generates avalanches of different amplitudes and duration, is definable a flicker, the overlap of these signals. It is possible to see the flicker as the overlap of periodic signals of different frequencies. The energy of each one of this frequency is proportional to $\frac{1}{f}$ where f is the frequency of the signal. For this reason the flicker is best known as $\frac{1}{f}$ *noise*: *noise* because of its apparent irregularity very similar to that of a classical noise, $\frac{1}{f}$ because inside the irregularity exists a precise ratio between signal frequency and its own energy.

According to Bak's theory the exponentiation and flicker law are characteristic not only of the pile of sand, but they are universal laws of all complex systems, of which the pile of sand is the most paradigmatic example.

Combining *SOC* dislocations model to our observations we obtain the following overview. Entangled dislocations form a rigid lattice, which contributes to elasticity. Dislocations can disentangle, in a domino effect, by local stress, mechanical oscillations or simply thermal fluctuations. Using the *SOC* model to explain dislocations disentanglement, we realize that material elasticity is reduced. Disentangled dislocations produce viscous – like effect, something like when you try to spread honey by knife on a biscuit. The eventual re – entanglement of dislocations in a different configuration can explain the observed static hysteresis (residual internal friction at zero frequency), while the adopted scale – free nature of the *SOC* model is able to explain the unexpected, but observed, 1/f slope of the GAS transfer function, since this additional dissipation process contributes to raise it [10]. I focused on the first aspect. A reasonable doubt may apply: could this description in term of avalanches contribute to internal friction at high frequencies?

Disentanglement is a slow process and, at frequencies higher than the avalanches characteristic growth times , there is not possibility to constitute an avalanche. Experimental evidence (lower observed losses) support this theory [9].

3.4 Geometric Anti Spring (GAS) and Electro Magnetic Anti Spring (EMAS) filters.

All seismic attenuation systems developed for gravitational waves interferometric detectors are constituted by a cascaded of harmonic oscillators with resonant frequencies below the frequency region of interest in such a way to realize a low pass filter. For the seismic isolation in the horizontal direction they are simple or inverted pendulums, as described in Chapter 2. Otherwise, for the vertical direction they are soft springs. All the interferometric detectors use cantilever blade springs except LIGO, which uses helical springs. Image to realize a mechanical isolator with a resonance at 300 mHz by means of a linear spring, the elongation of the spring would have to be about 3m. Until today several technical solutions have been studied and applied to solve this strong problem using magnetic repulsion force etc…[15]

Geometric Anti – Spring (GAS) is the solution developed for SAS (Seismic Attenuation System) adopted by Advanced LIGO and TAMA300, but also Naples VIRGO group laboratory has three "GAS towers". GAS filter realizes low frequency resonance, typically about a few hundreds of mHz, based on a linear anti – spring effect. The apparatus used in our experiment is the GAS filter, which is basically a second order passive mechanical filter.

The GAS filter is substantially a set of cantilever springs, arranged in radial way, each of about 38 cm in length, mounted from a common retainer ring structure and opposing each other via a central disk. The payload, to be isolated, is connected to the central part. The prototype used in SAS is the Monolithic GAS filter [16], (MGAS) so called simply because the blades and central disk are machined from a single flat sheet of Maraging steel. The blades are secured at 45° to the filter frame. Moreover the blades are completely flat when manufactured and flexed like a fishing rod under load. The 3.44 mm thick blades are composed of Maraging Marval – 18.
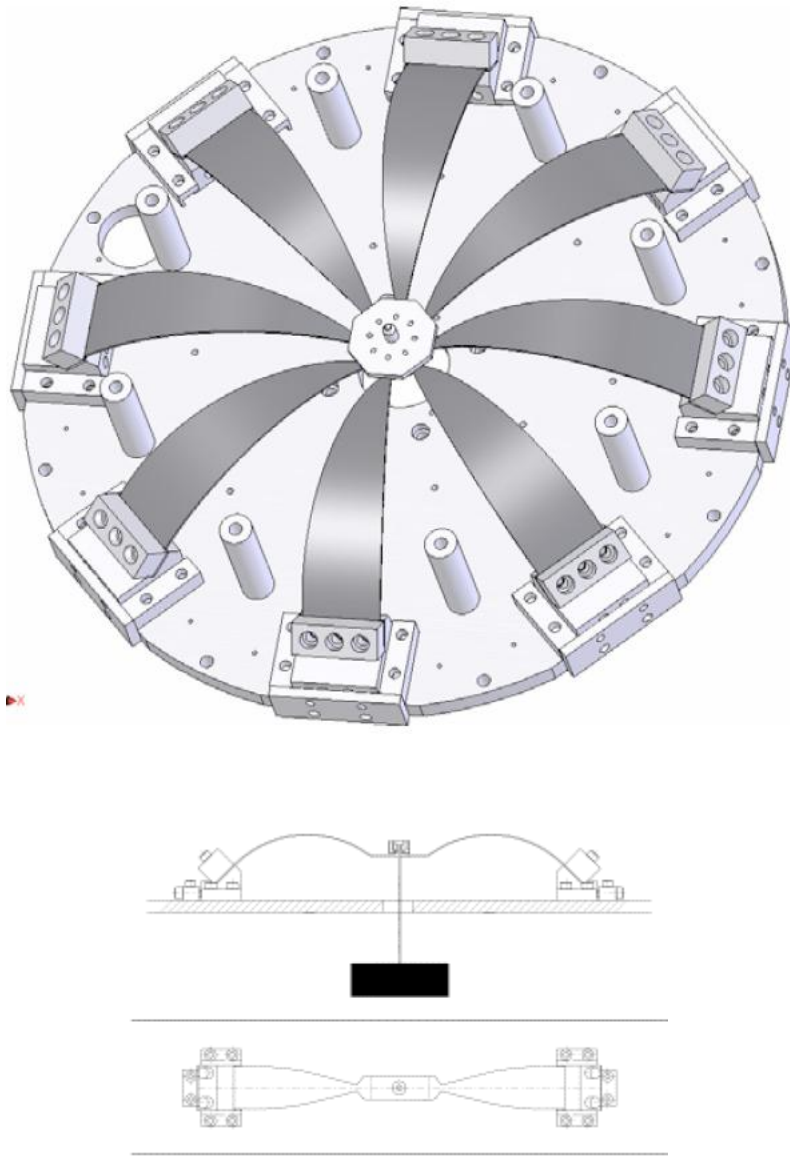
Figure 3.6: GAS filter, plant and side view. In this case we have 8 steel blades, but the working principle is the same.

To be honest, it should be necessary a numerical computation, with a sophisticated non – linear finite element model to describe the macroscopic behavior of the GAS. Nevertheless a simple and analytical model is satisfying to describe its working idea and to analyze its behaviors around its equilibrium (working position) with good precision.
Why this peculiar geometrical configuration?
Let's consider the adopted dynamic scheme for the GAS filter, sketched in the following figure:
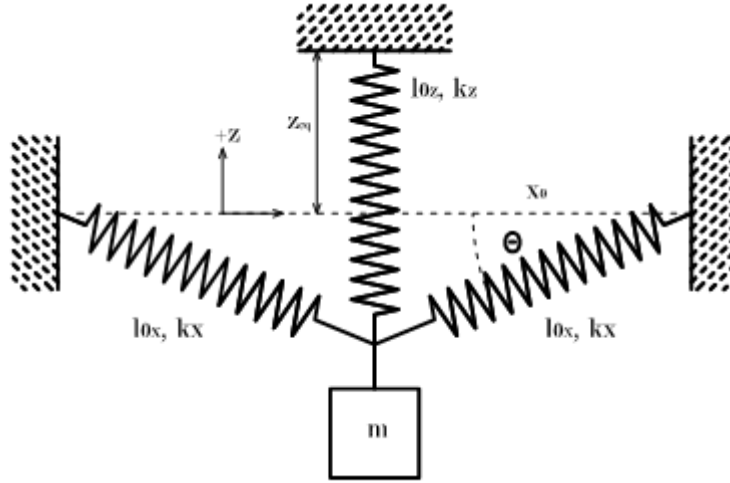
Figure 3.7: "Linear" model for the GAS filter.

Thanks to this model it is possible to understand that a long cantilever spring can be represented as a simple vertical spring with a horizontal component. In fact a set of springs tied at their tips can be represented as a linear combination of vertical and horizontal linear springs. The fishing – road bending of each blade is equivalent to a vertical spring, while the radial compression on the clamps is equivalent, according to this linear approximation, to the horizontal springs. Thanks to the particular symmetry of the system, the model shows dynamical equivalence to a single blade with the constraint that the tip of the blade can move only along the vertical axis, thus realizing the compensation of the horizontal component of the spring forces in the real system. Let's see in more details.

In this scheme the payload is suspended by a vertical spring of elastic constant k_z and rest length l_{0z} and by two horizontal springs of elastic constant k_x and rest length l_{0x}. The equation of motion for the system is [17]:

$$m\ddot{z} = k_z(z_{eq} - z - l_{0z}) - k_x(l_x - l_{0x})sin\Theta - mg \qquad (3.3)$$

where $l_x = \sqrt{x_0^2 + z^2}$ is the length of the horizontal spring and z_{eq} is the elongation of the vertical spring corresponding to $\Theta = 0$. Approximating $sin\Theta \approx \frac{z}{x_0}$ for small angles, eq. (3.1) reduces to

$$m\ddot{z} = k_z(z_{eq} - z - l_{0z}) - k_x\left(1 - \frac{l_{0x}}{x_0}\right)z - mg \qquad (3.4)$$

And at the first order the system has an effective spring constant

$$k_{eff} = k_z + k_x - \frac{k_x l_{0x}}{x_0} \tag{3.5}$$

The last term of eq. (3.4) is the Geometric Anti − Spring contribution, that introduces, as you can see, a negative spring constant into the system: the effective stiffness is thus reduced, and consequently the resonant frequency, just by compressing the horizontal springs. This is the principle of the linear anti − spring effect, and the name of GAS stands from the fact that the anti - spring is realized by taking advantage of a specific geometry of the cantilever blade assembly. What will happen when we move away from the equilibrium point?
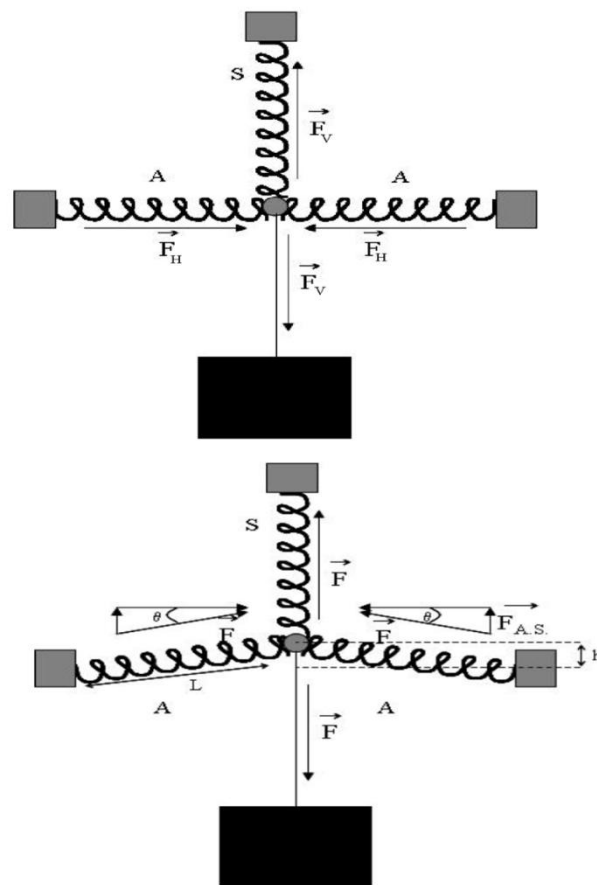
Figure 3.8: Overview about GAS mechanism running: in the equilibrium configuration (top) and moving out from it (bottom sketch) (courtesy of R. De Salvo)

At the working point, the two horizontal springs (A) carry no load, but they are radially compressed and their forces cancel. Moving away from the

equilibrium point(bottom) the compression of the A – springs results in a vertical force, proportional to the displacement, the *Anti – Spring force*. The Anti – Spring effect is proportional to the radial compression[9].

The GAS filter is used to null up 95 to 96% of the spring restoring force near the filter working point, giving in such a way the possibility to explore the low frequencies region. However, in order to decrease even more the resonant frequency of the filter, the Electro Magnetic Anti Spring (EMAS) mechanism [18] has been utilized. It is mounted in parallel to the vertical spring and its goal is the further reduction of the filter restoring force in such a way to have a lower achievable frequency.

The EMAS are composed by a Linear Variable Differential Transformer (LVDT), position sensor [19] feeding a not contacting Actuator (a coil acting on a loudspeaker magnet)[20] via a linear amplifier with variable gain (coil driver). The target of the damping actuator designed for Seismic isolation system of a GW interferometer is to provide the forces necessary for both damping and positioning. Both instruments are coaxially mounted to the load suspension wire as shown in the figure 3.9.
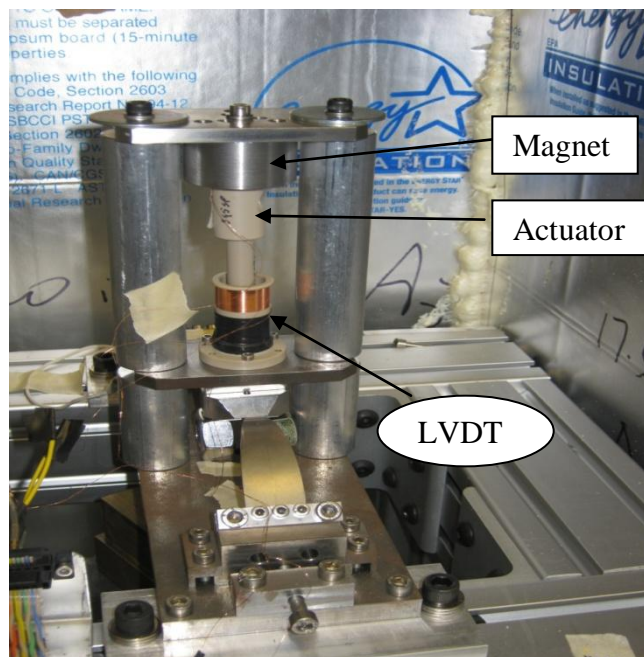

Figure 3.9: EMAS mechanism adopted

The LVDT is an electrical transformer used for measuring linear displacement. The transformer has three solenoidal coils placed end to end around a tube. The center coil is generally called *Primary*, while the outer coils are called *Secondaries*. A cylindrical ferromagnetic core, attached to the objects whose position has to be measured, slides along the axis of the tube. An alternating current is driven through the Primary, causing a voltage to be

induced in each Secondary proportional to its mutual inductance with the primary. The frequency is generally in the range $1-10$ kHz. As the core moves, these mutual inductances change, causing the voltages induced in the Secondaries to change.
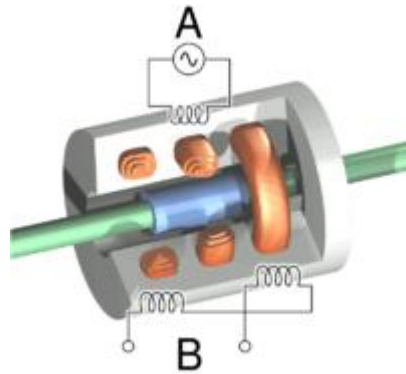

Figure 3.9: LVDT cross section showing the *Primary*, A, and

the *Secondaries*, B.

The Secondaries are connected in reverse series, so that the output voltage is the difference (hence "differential"). When the core is in its central position, equidistant between the two secondaries, equal but opposite voltages are induced in the Secondaries, so the output voltage is zero. On the contrary, when the core is displaced in one direction, the voltage in one coil increases as the other decreases, causing the output voltage to increase from zero to a maximum. According to the moving direction of the core, the output voltage is in phase with the Primary voltage or it is opposite to it. The most interesting property is the linearity response of the instrument: the magnitude of the output voltage is proportional to the displacement of the core (hence "linear") although inside a peculiar Voltage range as we will show. Because the core moves along the axis without touching the inside of the tube, there is no friction or rotating contacts making the LVDT a highly reliable device and perfectly sealed against the environment. The LVDT we used have been designed at Virgo as sensor for low frequency damping of Seismic Attenuation System. They are low – power, Ultra – High- Vacuum compatible and non – contacting position sensors with nanometer resolution [19]. Unlike conventional magnetic core LVDTs, this arrangement has no ferromagnetic components and does not generate the unwanted forces when exposed to external magnetic. Moreover the linearity is within 1% over the range [-10 mm, 10 mm].

The EMAS is able to lead the oscillator to zero frequency with a negative spring constant k_{emas} or, by inverting the sign of k_{emas}, to increase the resonant frequency of the spring (k_{emas} is proportional to the EMAS gain, set in the feedback program, by a constant in N/m proportional to the actuator

efficiency). The same LVDT is used to monitor the system and through a Labview control program. As side − effect , the reduced restoring force makes the spring more temperature sensitive, but, the same actuator will provide a thermal compensation force.

In conclusion, thanks to the combined action of the GAS and EMAS filters, the restoring force of the spring is almost completely nulled: we have built our personal microscope to explore the dissipation dynamics that occurs inside the Maraging and Glassy metal blades.

Chapter 4

Experimental approach and data analysis

4.1 Experimental setup

The experiment has been performed in a sub − basement laboratory at Caltech. We mounted two models of the GAS filter side by side: one made by Maraging blades and one made by Glassy metal. Our GAS filter prototype is based only on two blades, but its working principle is the same of the one already described in the previous chapter. Because of the different Young's modulus of the two materials ($E_{Maraging} = 210\ GPa$ and $E_{LM001} = 96\ GPa$) the payload is different for the two prototypes. Glassy metals, being more elastic, allow the application of more strain and therefore allow for ticker blades in the same geometry. Because the load changes with the cube of the thickness we have a load of 18.0 kg for the Glassy metal GAS filter and a load of 9.3 kg for the Maraging GAS filter.
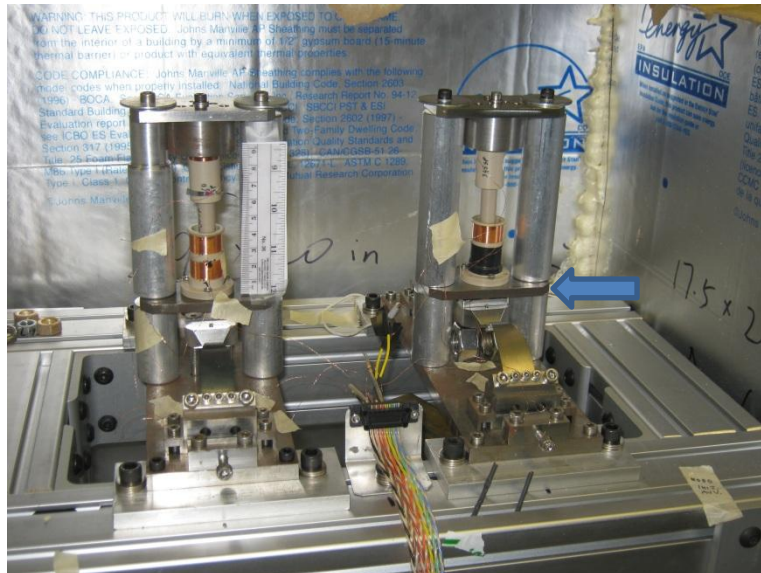

Figure 4.1: Maraging and Glassy metal prototypes.

Figure 4.2: Different load for the two systems.

The main sources of perturbations inside the laboratory were due to the turbulent air currents and thermal cycles from the air conditioning systems (we noticed a variation of about 2 °C during a week with most hourly cycling periods). For this reason we built a box around the experiment, made of faced aluminum foil, 5.2 cm thick, rigid polystyrene foam panels welded together in a cube. In such a way we reduced the thermal fluctuations to less than one degree and we impeded most of the air conditioning flux. We also added thick rubber foam strips to create an air flow barrier. A thermal fluctuations of less than a degree centigrade was anyway too high for our goals: the thermal drift of the filter was of the order of one mm/°C, while the effects we are investigating for could be on a submicron scale. For this task an active thermal compensation was introduced. This feedback kept the filter at its optimal working point, which corresponds to the height where the Anti-Spring effect is maximized. The working mechanism of the thermal compensation was the following: the LVDT was used to acquire the filter displacement signal from its working point, then an Infinite Impulse Response (IIR) feedback integrator continuously integrated it and fed it to the vertical actuator's coil, which, acting against the magnetic field of the permanent magnet, generated the thermal compensation force. During the day, traffic and lab activities all around, resulted in significantly higher and changing disturbance levels. Since our presence in the room affected the spring's stability (we noticed during the Actuator calibration that the number of people in the laboratory and even the open door was a significant noise source) we implemented remote controls of the experiment and performed all critical measurements remotely and preferably during the night. Nonetheless

residual air turbulence and its resulting fluctuating pressure, acting on the spring surface, remained the main sources of disturbances during the night.

The block diagram of our experiment with the different paths for each component is the following:
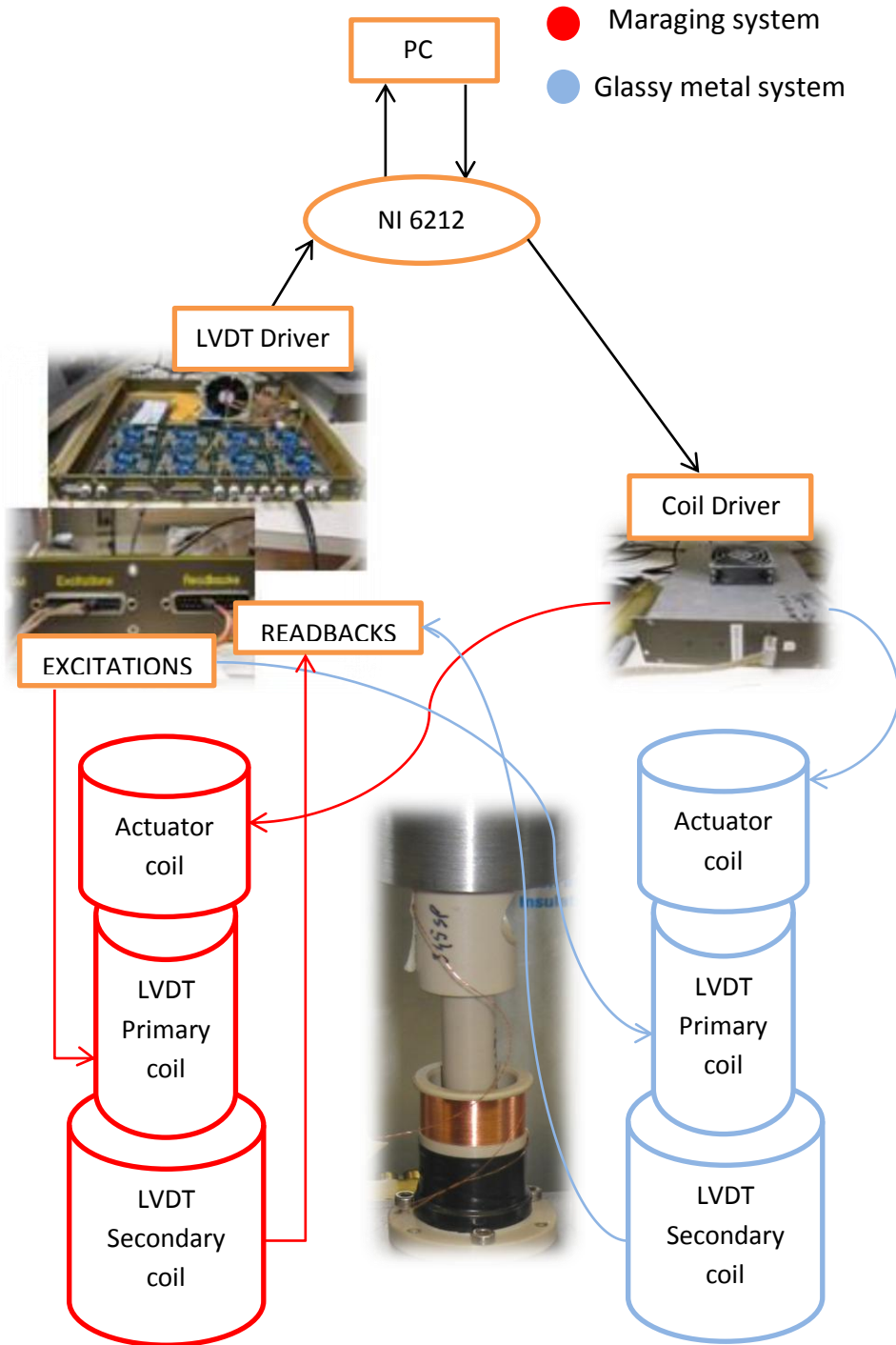
The *LVDT DRIVER* has been a key instrument for our experiment: it had 8 channels and it allows position readout with few nm resolution over a mm scale. Each channel separately provided the excitation signal for the primary

coil of a single LVDT and read the voltage from the secondary coils of the same LVDT. An integrated Voltage signal, proportional to the position was acquired on an ADC card. The frequency of the signal of the primary coil was of 10kHz.

The LVDT driver overheating was a not negligible problem: after few hours it was so hot that it started to fail. To solve this problem we first soldered a little fan inside the LVDT driver box, which introduced a noise that altered the readout signal. We put on each operational amplifier of our working channels a screw by thermoconductor tape obtaining the required cooling without additional noise. The actuator too seemed to get hot and for this reason we soldered a little resistor (35 Ω) in series with the coil it drives to decrease the current.

The *COIL DRIVER* was a x10 power amplifier. It received the control signal from the computer controlled DAC in a NI 6212 Card and sent it to the actuator coil, after amplifying it.

To give an idea about the connection – diagram it is possible to take a look to the Appendix.

The DAC output is subjected to digitalization noise, to different degrees, according to the different resolution scale of this instrument. The DAC had ±10 V output, while a coil driver ±1V input. Adding a resistive voltage divider in series according to scheme proposed in the Appendix, we reduced the output scale and its digital noise by about a factor of 10.

4.2 Preliminary tuning and calibrations

As we have already discussed, the GAS filter is optimized at the height where the radial compression of the blades is maximized. To determine the optimal working point we monitored the spring's movement with the LVDT and progressively added little nuts on the system. To be precise there were two ways to change mass on the system. One was to add small nuts on the load and the other was increasing the current sent to the actuator by using the Labview program in such a way to change the excitation force obtained through the actuator. We chose the first one. The "starting mass load" was 1.8 kg for the Glassy metal system and 9.3 kg for the Maraging system. Each nut was dropped from a given height to excite the spring's oscillation with a controlled amount. Each step generated a ring down. For each added nut we recorded the oscilloscope's signal, the frequency and the mean voltage of the signal as estimated by the oscilloscope internal functions. The first evaluation from the oscilloscope estimations was followed by a better precision one obtained from the stored data using the damped sinusoidal function fit:

$$h + A\,e^{\frac{-(t-t_0)}{\tau}}\,sin[2\pi f\,(t-t_0)]$$

(4.1)

55

Chapter 4. Experimental approach and data analysis

where h is the oscillation mean height (the spring's equilibrium point), A its amplitude, f the oscillation frequency, t_0 a phase taking account the startup time and τ the decay lifetime.

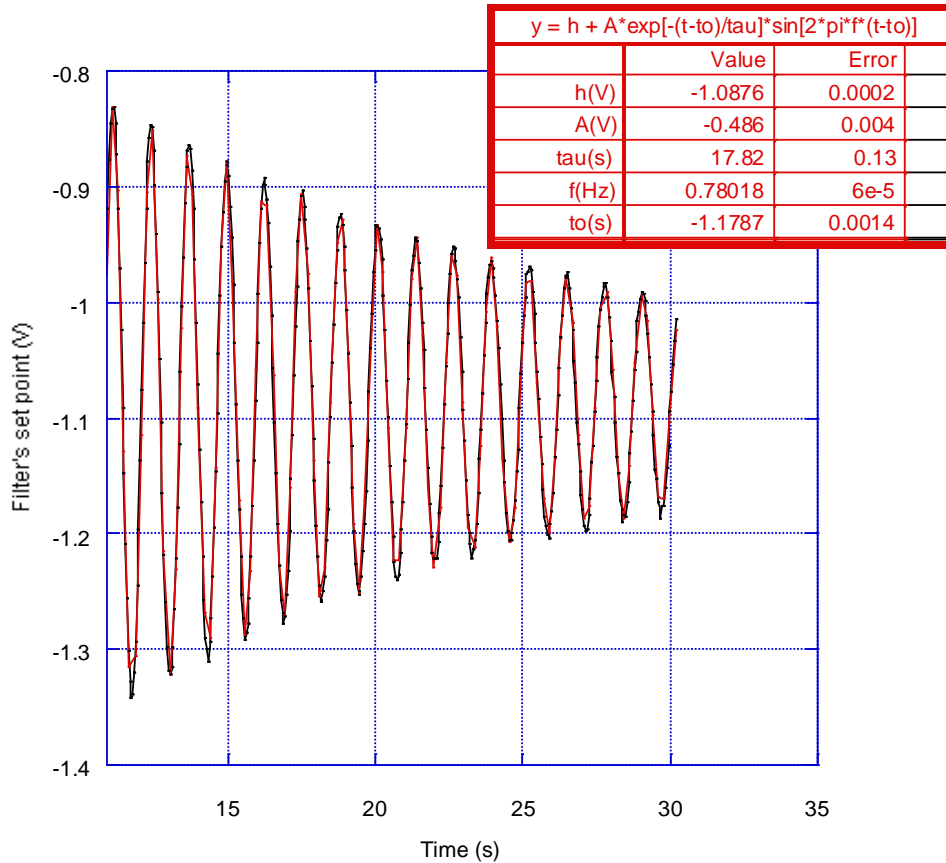An example of the fitting procedure (we used KaleidaGraph program to do it) is shown below:

$y = h + A*exp[-(t-to)/tau]*sin[2*pi*f*(t-to)]$		
	Value	Error
h(V)	-1.0876	0.0002
A(V)	-0.486	0.004
tau(s)	17.82	0.13
f(Hz)	0.78018	6e-5
to(s)	-1.1787	0.0014

Figure 4.3: A ring down (black points in the plot) has been fitted with the damped sinusoidal function fit (eq. 4.1, red line in the plot) to find the filter resonance frequency f, its height h and its lifetime τ. In this example the filter oscillates around a set point of about − 1 V.

With different mass load the GAS filter achieves different equilibrium point, readable, through the LVDTs, as different mean voltages. By plotting frequency versus mean voltage (fig. 4.4) it is possible to find a parabola, whose minimum corresponds to the wanted maximum compression of the GAS filter. Following the Dirichlet's theorem, the minimum point is a stable equilibrium point for the system.
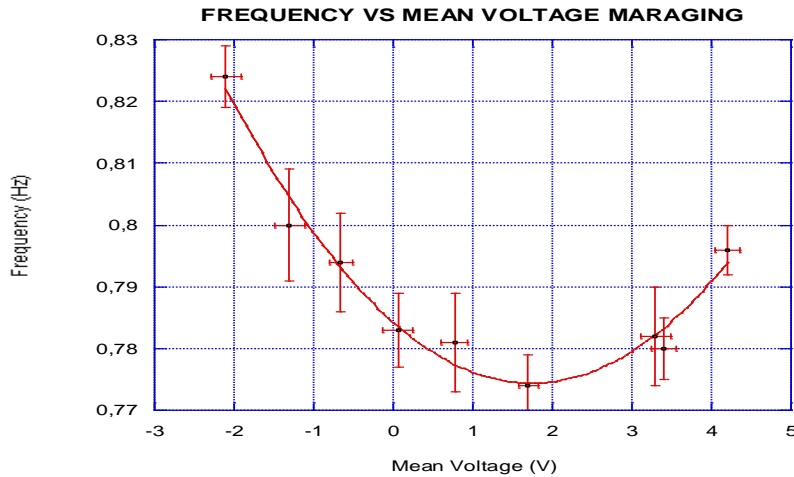
Temperature: 23.6 °C, Minimal point frequency: (0.772±0.002) Hz,
Minimal point mean voltage: (−1.68±0.19) V
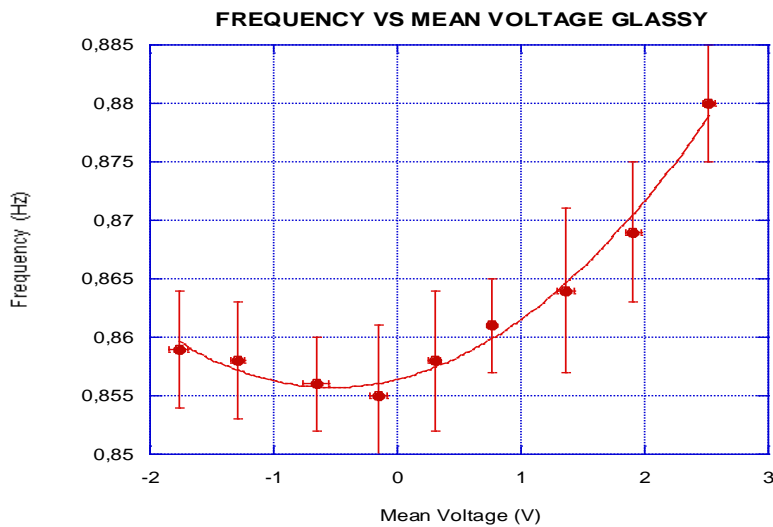
Temperature: 22.1°C, Minimal point frequency: (0.8552±0.0006) Hz,
Minimal point mean voltage: (−0.52±0.08) V.

Figure 4.4: Scanning of the spring around its best working point to find the minimum point of the parabola corresponding to the maximization of the GAS effect for both the prototypes.

We want to mechanically zero the readout position of the LVDT at the minimum point to take full advantage of the range of the LVDT driver that has an output limit of ± 10 V and to ensure our LVDTs were working inside their linear dynamic range. For this, we first added shims on the two cylinders under the plate (indicated by the arrow in figure 4.1) to change the

height of the emitter coil until zero output is obtained. Knowing the precise value for the height, we could machine the cylinders with height corresponding to $\cong 0$ V at the minimum point. In the glassy case we were lucky because the minimal point mean voltage happened just about at 0 V, while in the Maraging case we obtained the following linear relationship at a temperature of 23.62 °C:

$$V = -\ 5.42 - 8.69h \qquad (4.2)$$

Where V is the mean voltage and h the height. From it:

$$\Delta V = -8.69\Delta h \qquad (4.3)$$

that means 1mm corresponds to $-8.69\ V$ or that 1 V corresponds to -0.115 mm. After machining the correct height cylinders we plotted again frequency versus mean voltage for the Maraging system obtaining this time:
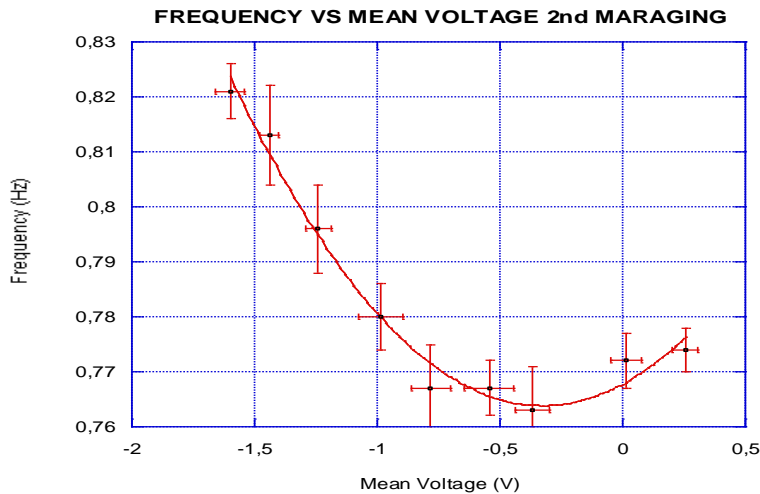
Temperature: 22.6°C, Minimal point frequency:(0.764±0.004)Hz, Minimal point mean voltage: (–0.33±0.09) V.

Figure 4.5: Second scanning of the Maraging springs around its best working point. Let's note the minimum point mean voltage at –0.33 V, after the machining of the cylinders with correct height.

We needed to know exactly the added masses to put on the load (starting masses) corresponding to the best working points. For this reason we plotted mean voltage versus added masses and then we extrapolated the right mass of the working point.

MEAN VOLTAGE VS MASS MARAGING
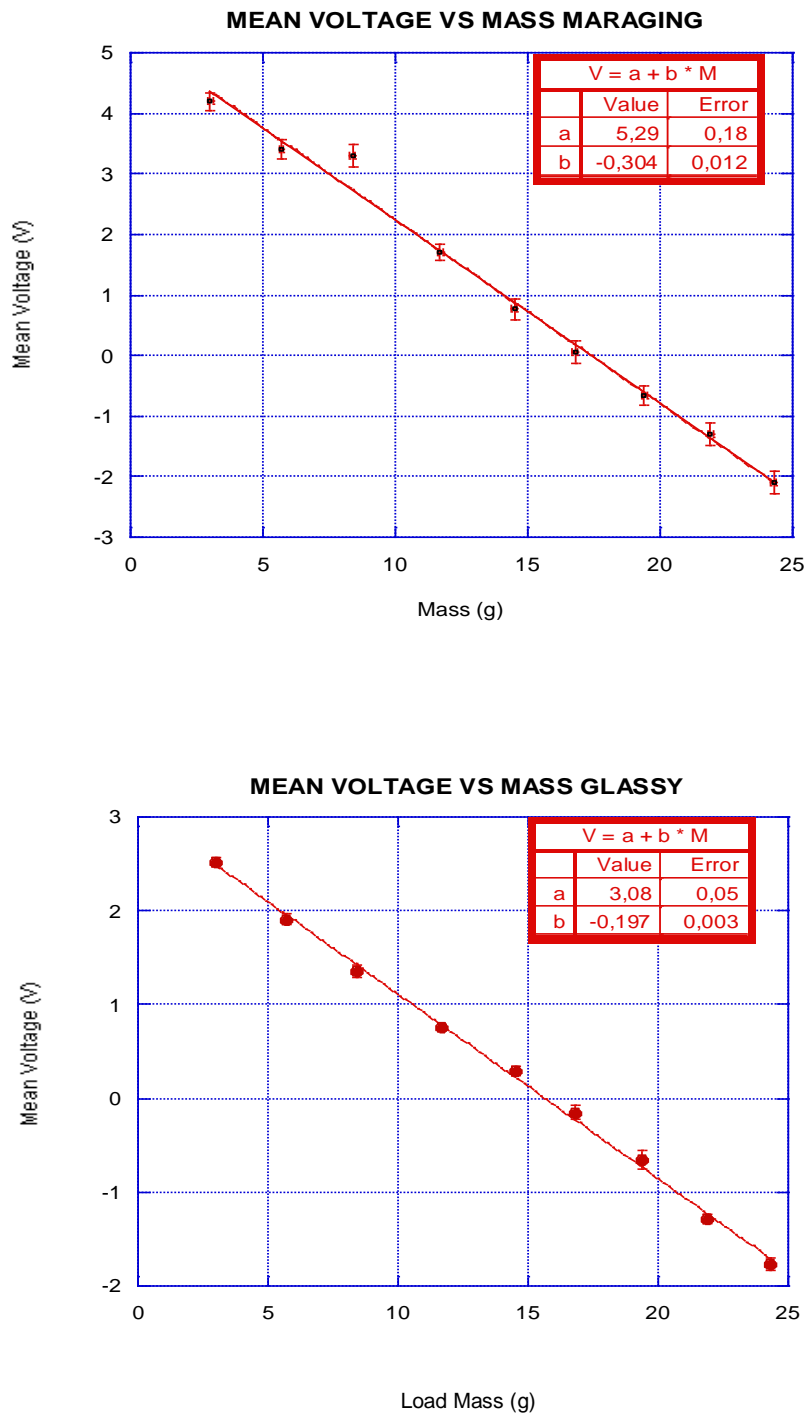

MEAN VOLTAGE VS MASS GLASSY

Figure 4.6: Finding the added mass of the best working point.

In conclusion we found:

Maraging balancing mass of the minimum frequency point: (18.5 ± 1.6) g.

Glassy balancing mass of the minimum frequency point: (18.3 ± 0.9) g.

Once the correct balancing mass was determined, we didn't change it anymore.

After that the mounting process and the working point finding were successfully ended we started the fine calibration of ours LVDTs and actuators. The LVDT fine calibration was (4.40 ± 0.10) V/mm for the Maraging system and ($- 6.56 \pm 0.12$) V/mm for the Glassy metal system. It was done adding little nuts of known weight on the load and reading, every time, both the blade's height on a ruler and the mean voltage by the oscilloscope. To avoid the parallax error we mounted a fixed web camera (figure 4.7) in front of the ruler making a photo for every nut added. Then with the help of paint program, we interpolated between the 1 mm marks of the ruler, thus obtaining very precise readings of the height of the springs.

Figure 4.7: Proceedings adopted for the LVDTs calibration. The fixed camera (left on the top photo) stares at a stationary ruler and at a needle attached to the moving part of the GAS spring.

Chapter 4. Experimental approach and data analysis

The resulting LVDTs fine calibration plots are shown below:

MEAN VOLTAGE VS HEIGHT ON THE RULER

V = a + b * h		
	Value	Error
a	-298	7
b	44	1

V = a + b * h		
	Value	Error
a	-298	7
b	44	1

MEAN VOLTAGE VS HEIGHT GLASSY

V = a + b * h		
	Value	Error
a	402	7
b	-6.56	0.12
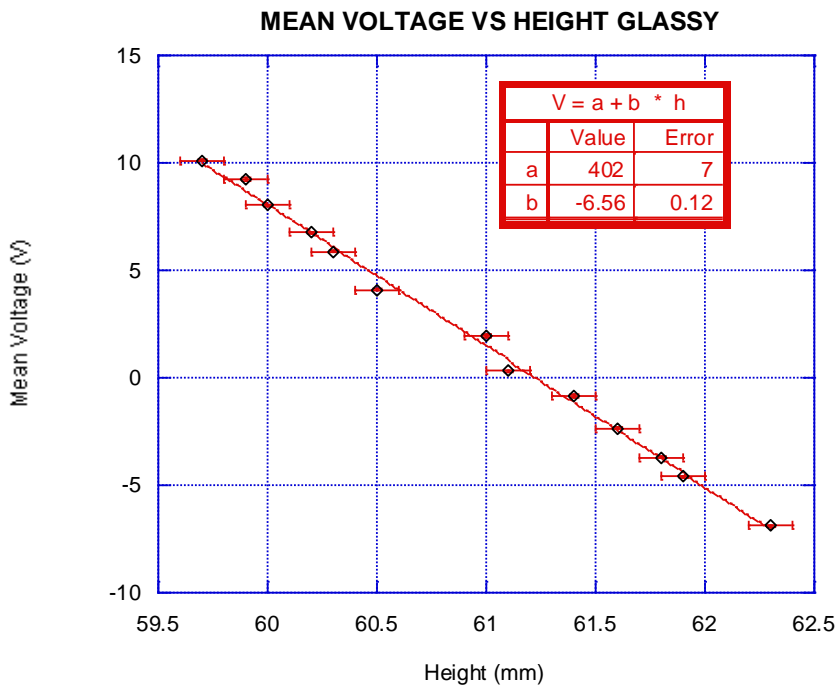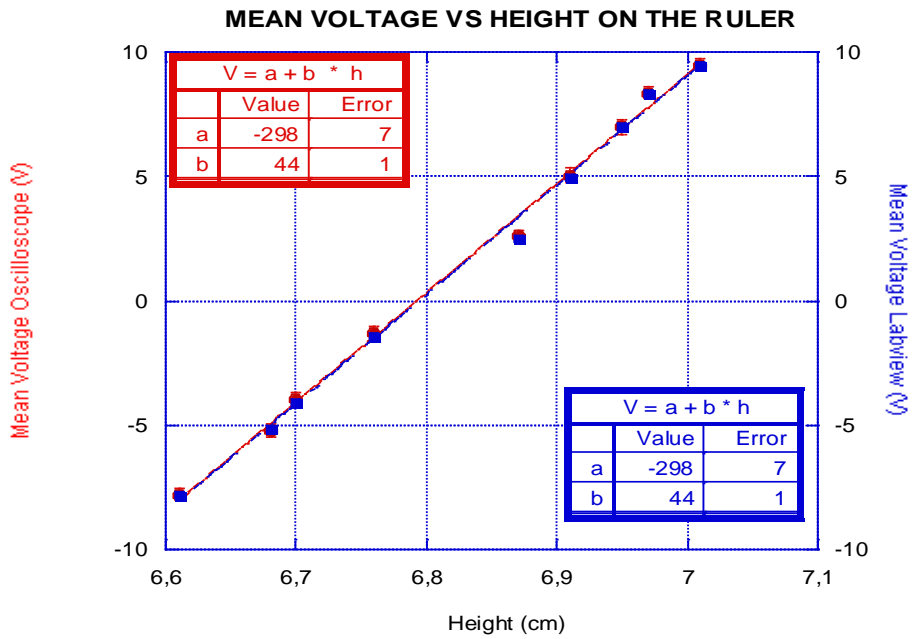
Figure 4.8: LVDTs calibration. In the case of the Maraging (top plot) we measured the mean voltage through both oscilloscope and Labview program, obtaining comparable results.

61

The actuator fine calibration, $(- 12.67 \pm 0.16)$ mN / V for the Maraging system and $(- 1.21 \pm 0.07)$ mN / V for the Glassy system, was performed by first staring a feedback program holding the program at its pre – determined working point, and then adding and subtracting known masses (the little nuts of about 0.6 g or 0.8 g each) and measuring the voltage required by the feedback to return the system to the optimal working point. Because of the already observed springs hysteresis, we run the measurement by first adding all the masses one by one, and then by subtracting them.

The fits of figure 4.8 determine the conversion parameters for the control program in which the LVDT voltage signal is converted to millimeters according to the equation: LVDT(mm) = a * LVDT (V) + b and the actuator voltage (V) required by the feedback to return the system to its best working point to a force F in mN according to the equation: F(mN) = a * Voltage(V) + b, where a e b are the slope and intercept determined by the fits of figure 4.9.
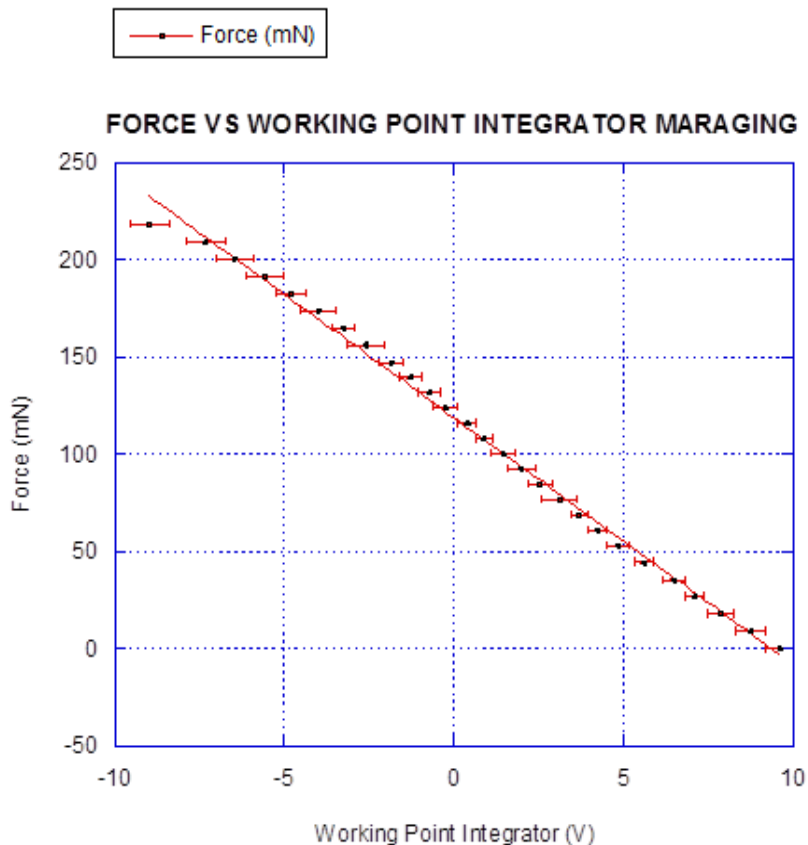
F = a + b * V		
	Value	Error
a	118.6	0.8
b	-12.67	0.16

FORCE VS INTEGRATOR WORKING POINT GLASSY

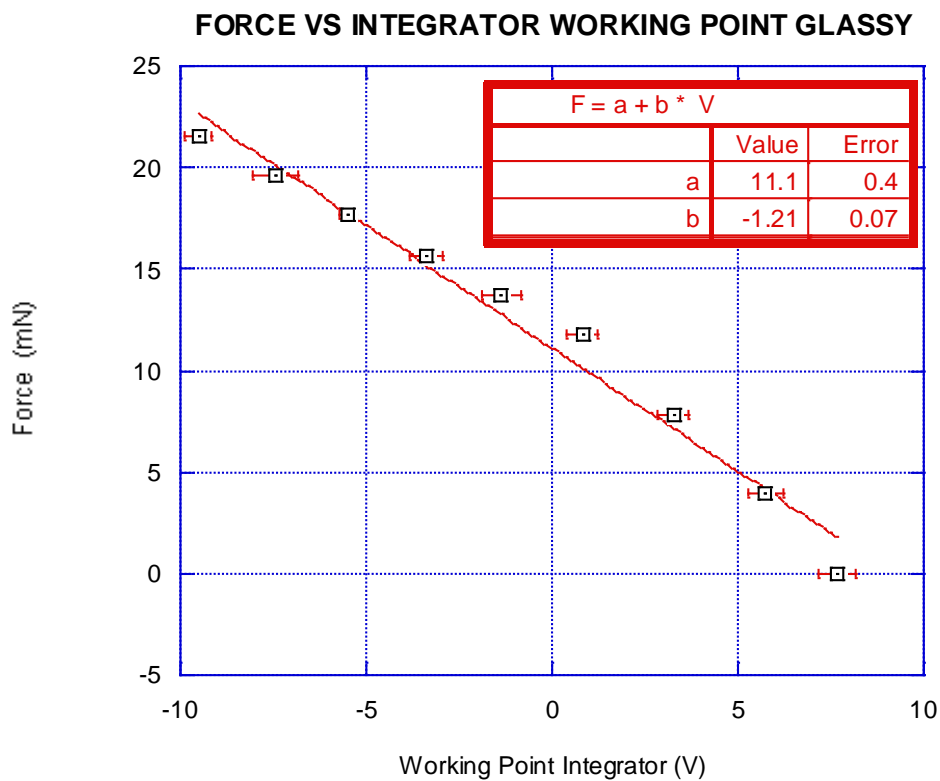| F = a + b * V		
	Value	Error
a	11.1	0.4
b	-1.21	0.07

Figure 4.9: Actuators fine calibration for both the systems.

4.3 Hysteresis testing

The EMAS mechanism is particularly effective to explore the effects of hysteresis at low frequencies because it allows   to remotely change the filter's resonant frequency theoretically all the way to zero (mathematical region of instability), without changing the stress in the system and without losses. The EMAS gain of the feedback system is equivalent to a variable spring constant. The expected resonant frequency will follow the formula:

Chapter 4. Experimental approach and data analysis

$$f = \frac{1}{2\pi} \sqrt{\frac{k_0 + k_{EMAS}}{M}} \qquad (4.4)$$

where M is the payload mass of the system, k_0 is determined by the GAS tune of the filter (it is the usual spring constant $k_0 = \omega^2 M$) and k_{EMAS} is equal to the EMAS value set in the feedback program, that we will name EMAS gain, multiplied by a constant proportional to the actuator efficiency. The EMAS mechanism is able to drive the oscillator all the way to zero frequency or, with positive k_{EMAS}, to higher frequencies.

We fitted resonant frequency versus Emas Gain according to the (4.4) giving an estimation for the value of the constant thus obtaining the value of k_{EMAS} , as shown in fig. 4.10:
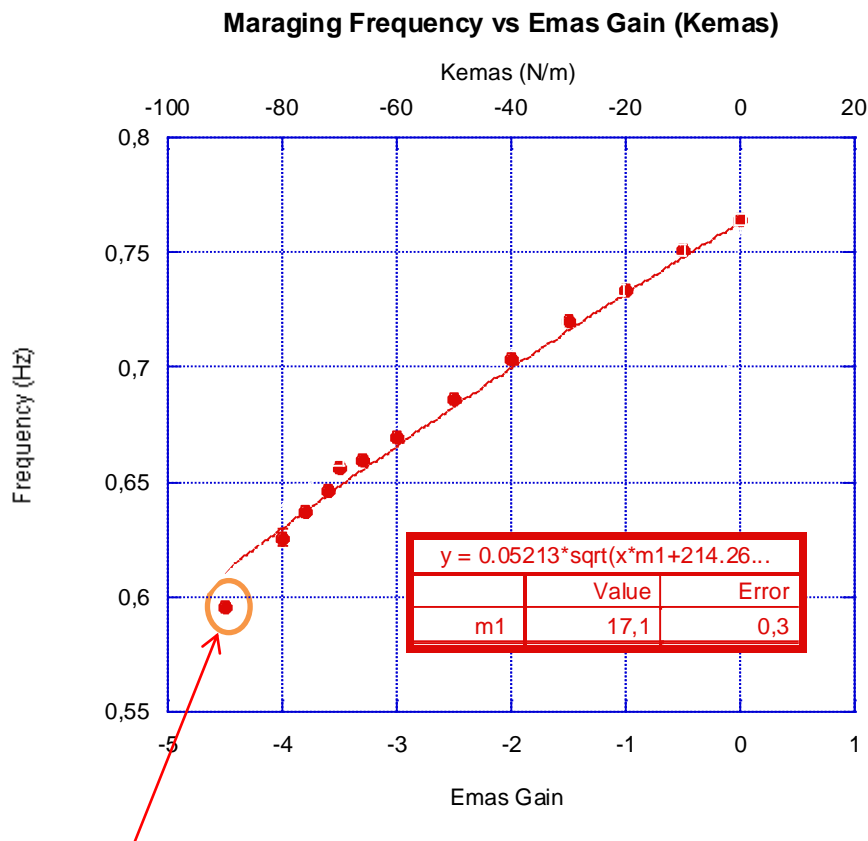
Let's note this experimental point deviating from the fit. The most realistic reason about its deviation is the not so clear signal from which it was extracted. In fact, the signal was obtained through Internet connection (Timbuktu program) which didn't give a continuous signal.
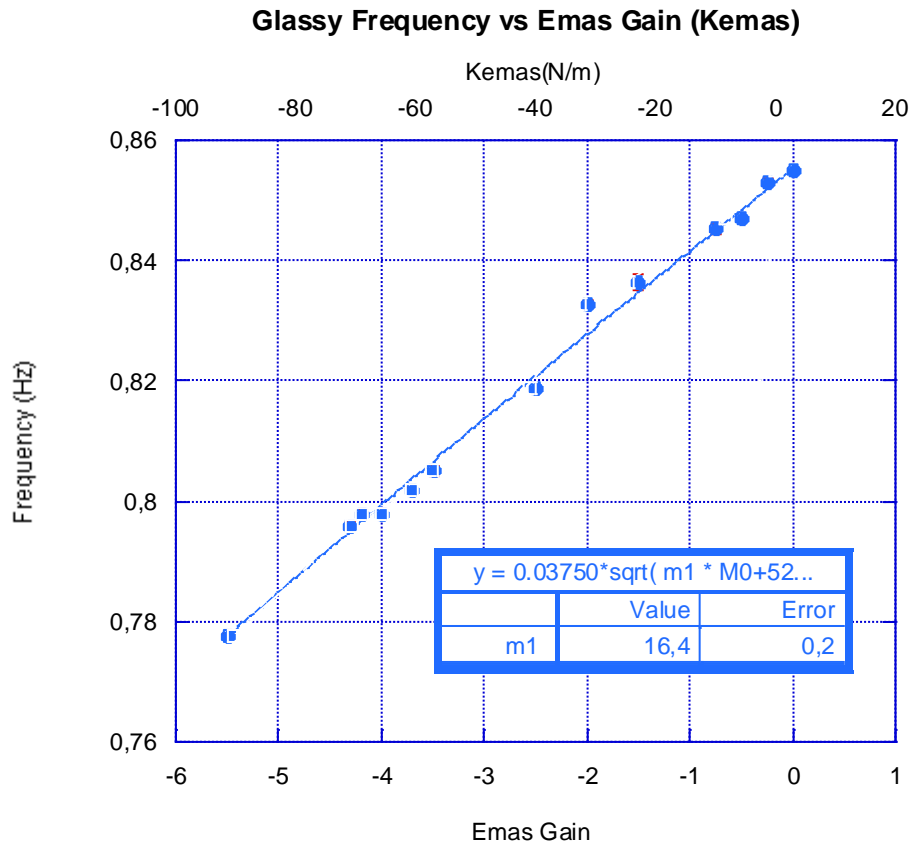
Figure 4.10: Filter frequency versus Emas Gain (k_{EMAS}) for both the systems.

From the fit we found:

MARAGING CASE:

$$k_{EMAS} = EMAS\ GAIN * 17.1\ N/m$$

Thus obtaining $k_{EMAS} = (-8.6 \pm 0.3)N/m$ for EMAS GAIN = - 0.50.

GLASSY METAL CASE:

$$k_{EMAS} = EMAS\ GAIN * 16.4\ N/m$$

Thus obtaining $k_{EMAS} = (-8.2 \pm 0.2)N/m$ for EMAS GAIN = - 0.50.

The hysteresis measurements were performed at two different EMAS gain, starting from a $k_{EMAS} = 0$ which corresponds, according to the (4.4), to a

resonance frequency of 0.764 Hz for the Maraging system and to 0.8552 Hz for the Glassy system. A recent study[8] shows that only applying alternated sign excitations to the system it is possible to observe hysteresis in the GAS filter displacement. Moving from this consideration we applied to the actuator a voltage generated by an *Auto Pause Cos function* (fig. 4.10) defined by the function:

$$Auto\ Pause\ Cos\ function = \frac{-[A\cos(2\pi f t)-1]}{2} \qquad (4.5)$$

Where A is the amplitude of the signal, f its frequency and t the time. Why did we need this function? Auto Pause is manually started and it stops at all maximum and minimum of the sinusoidal signal and it is manually re − started. The function is used to generate slow force excitations and it allows the measurements of the hysteresis at the endpoints of an excitations cycle. In other words, we apply a force to the system, which slowly gets to a required value, pauses, then slowly returns to zero. To have a step rise much slower than the characteristic time of the oscillators ($\frac{2\pi}{\omega}$) we use a sinusoidal step transition of about $\frac{1}{30^{th}}$ of the resonance frequency of the system.

Hysteresis is a memory of the past positions: for this reason we repeated each step at certain amplitude (determined each time considering that the program has a limit of about $\pm\ 10$ V) 3 or 4 times in sequence. By averaging the positions of the LVDT signal immediately before the step up, immediately before the step down (at the highest amplitude), and after the step down, each time waiting about 3/5 minutes after the step until the signal is quite flat, we were able to determine both the actual amplitude of the system movement for each EMAS and its hysteresis, which is given by the difference between the position before and after each double step. The procedure was repeated with alternated sign. We estimated the hysteresis percent through the slope of the plot "Difference between the position before and after each full step versus Amplitude".
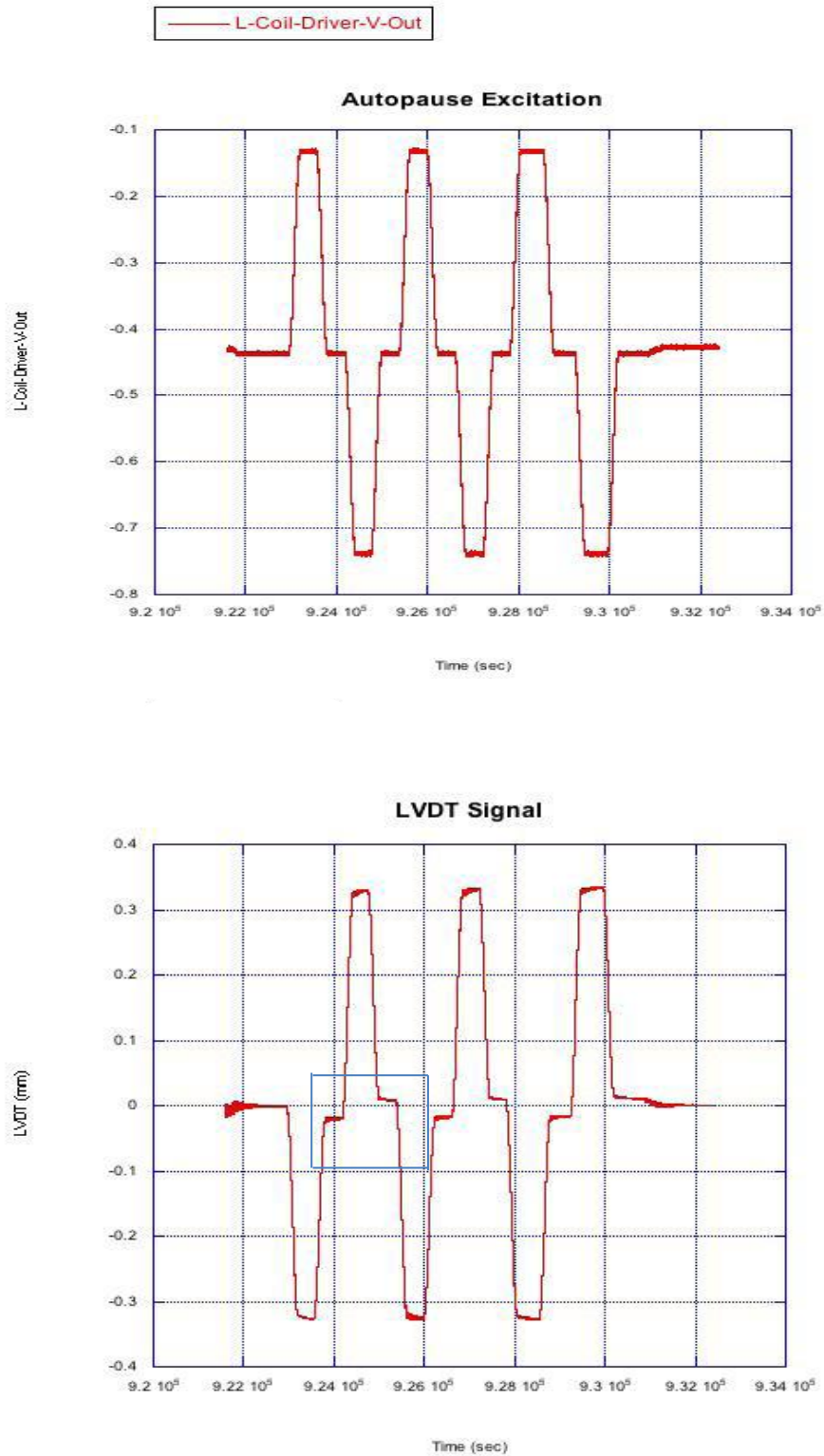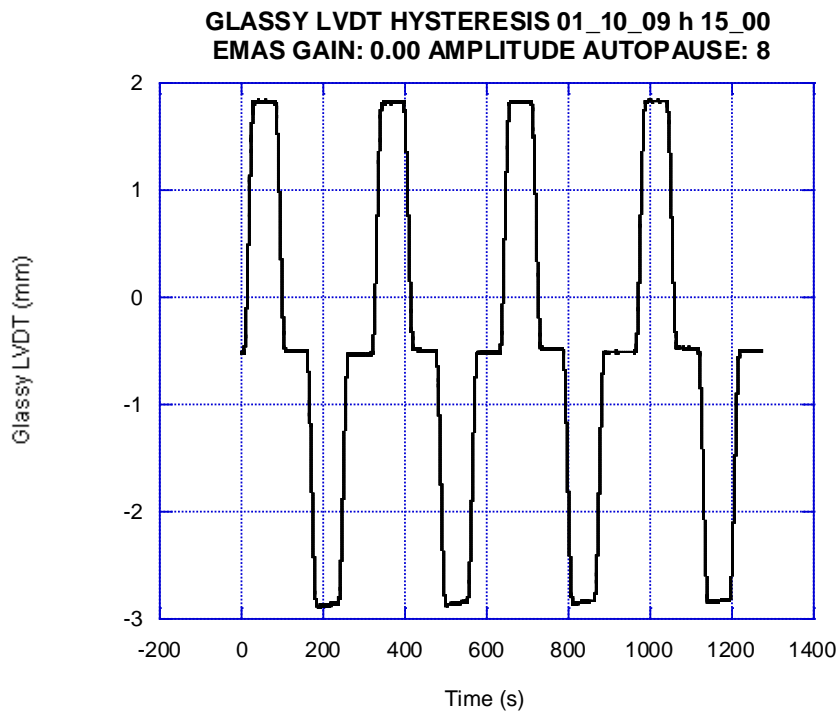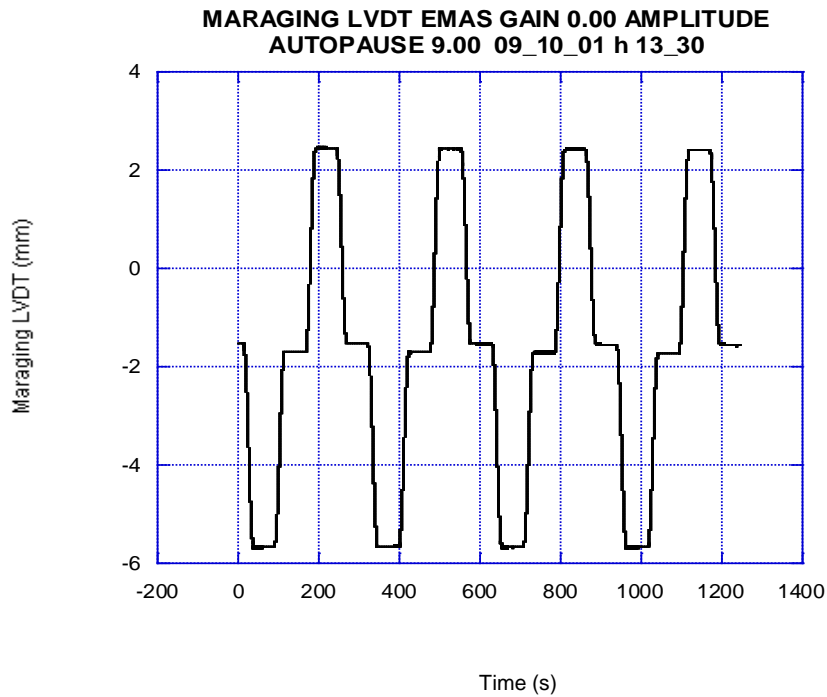
Figure 4.11: Example of the Auto Pause Cos in the top graph. The excitation signal that it generates slowly goes up and, stops and then goes down to zero and stops again, and repeats it with opposite sign. We expect and observe hysteresis to show up at every step, as it is evident in the square marked in the second graph.

Chapter 4. Experimental approach and data analysis

It is now interesting to compare the hysteresis for both the systems at the same EMAS gain. Below it is shown a compared plot with an EMAS gain = 0:

**MARAGING LVDT EMAS GAIN 0.00 AMPLITUDE
AUTOPAUSE 9.00 09_10_01 h 13_30**

Time (s)

**GLASSY LVDT HYSTERESIS 01_10_09 h 15_00
EMAS GAIN: 0.00 AMPLITUDE AUTOPAUSE: 8**

Time (s)

Chapter 4. Experimental approach and data analysis

To have a more clear idea about hysteresis difference it is necessary a zoom in which it is marked the different grade of hysteresis that will be confirmed quantitatively later (fig. 4.12):

Compared plot between Maraging and Glassy showing Hysteresis with Emas Gain 0.00
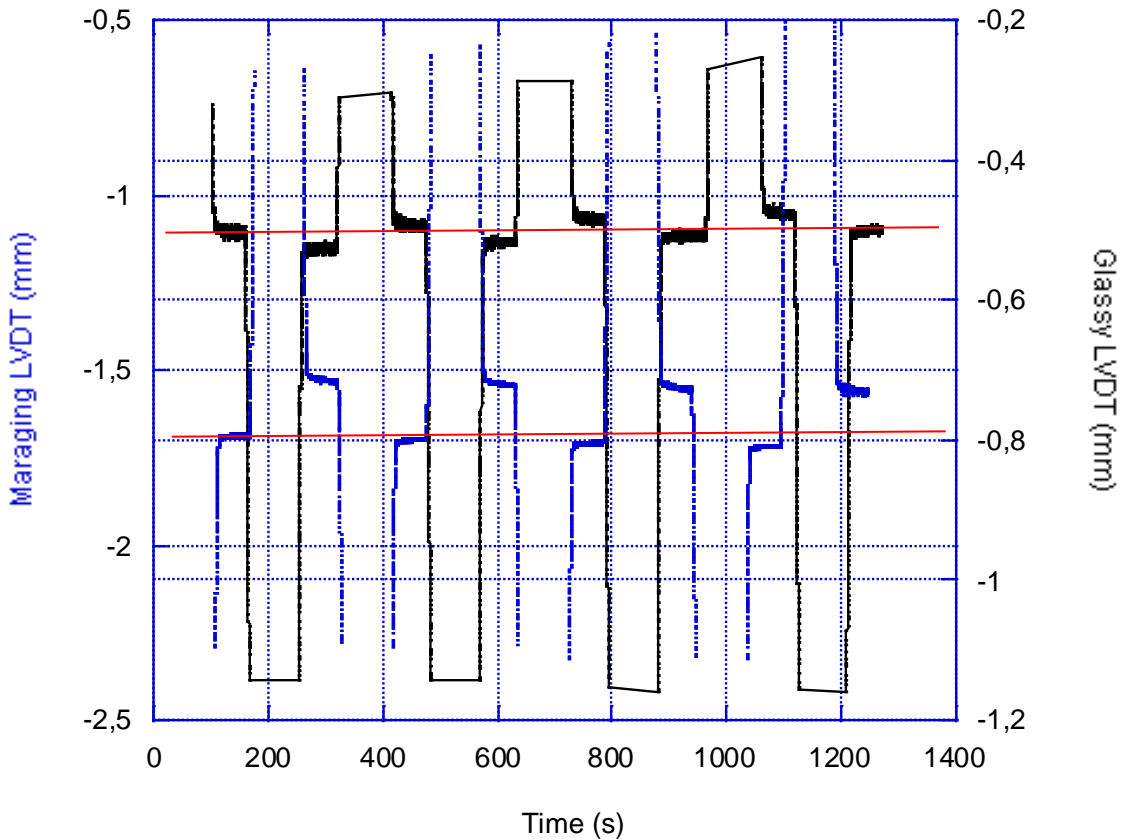
What is immediately evident is that there is less hysteresis with Maraging than for Glassy metal flexures. This is a clear signal that the two materials behave differently and worth much deeper investigation.

To achieve this goal the procedure was repeated with the same mechanical tuning for two different k_{EMAS} (EMAS GAIN = 0.00 and EMAS GAIN = -0.50 for both the systems), corresponding to progressively lower resonant frequencies.

Maraging Difference of Means vs Amplitude emas gain 0.00

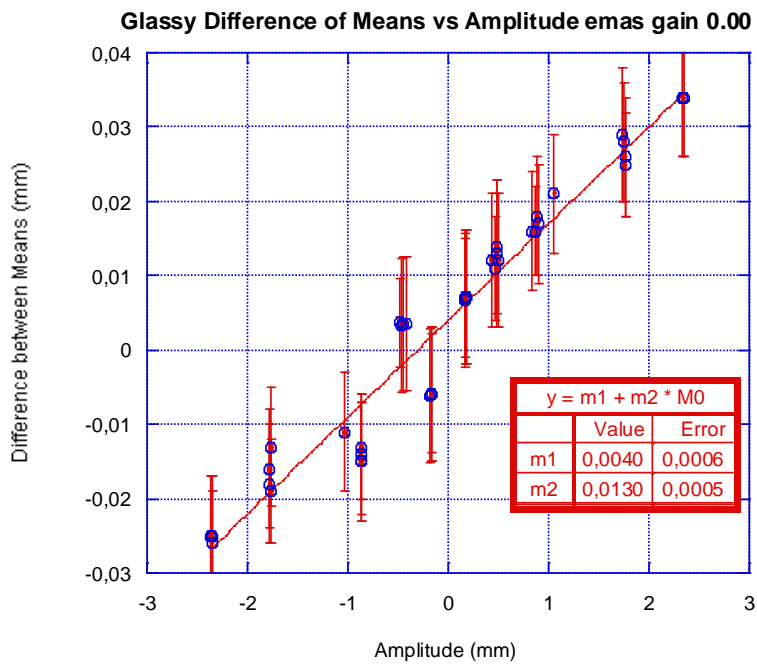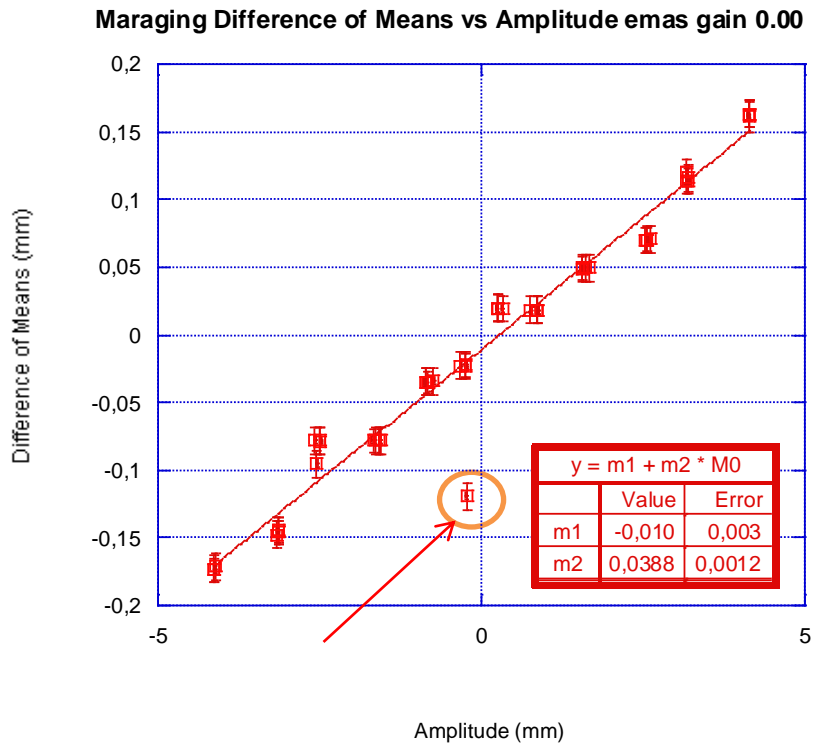**Glassy Difference of Means vs Amplitude emas gain 0.00**

Figure 4.12: Difference of means versus Amplitude for both the systems with an EMAS Gain = 0.00.

Maraging Difference of Means vs Amplitude emas gain -0,50

y = m1 + m2 * M0		
	Value	Error
m1	-0,009	0,003
m2	0,0382	0,0011

Glassy Difference of Means vs Amplitude emas gain -0,50

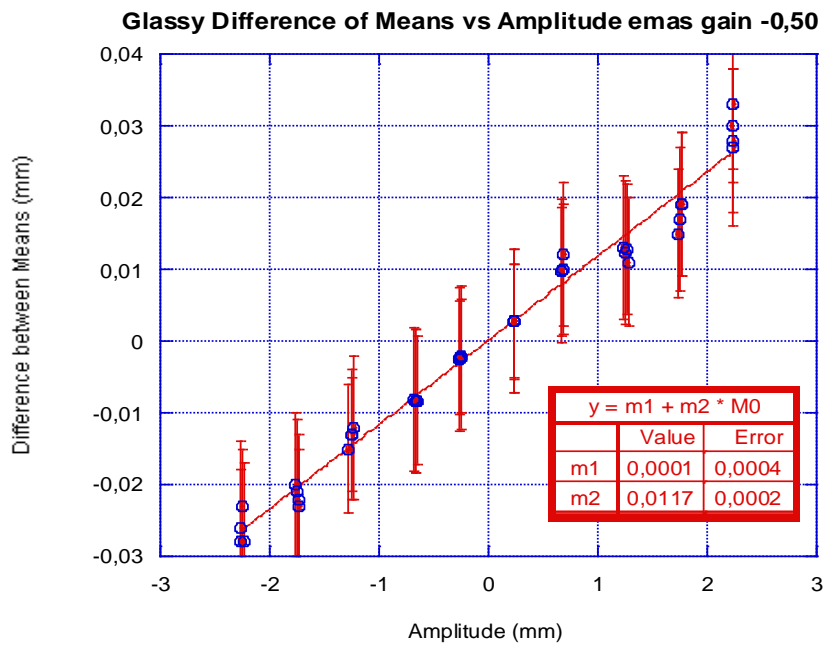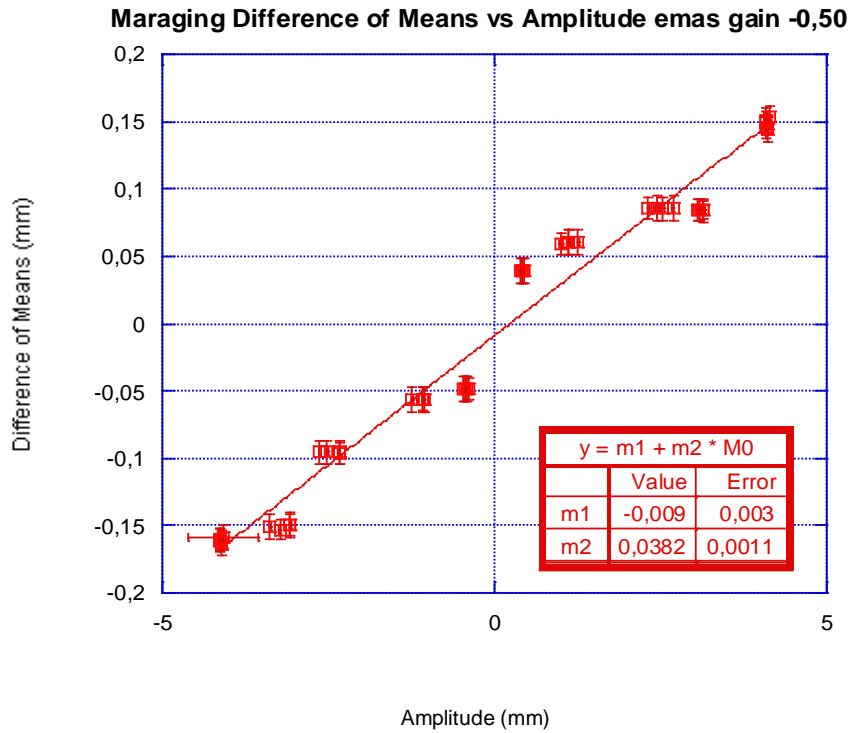| y = m1 + m2 * M0		
	Value	Error
m1	0,0001	0,0004
m2	0,0117	0,0002

Figure 4.13: Difference of means versus Amplitude for both the systems with an EMAS Gain = −0.50.

Chapter 4. Experimental approach and data analysis

The fits to the four graphs show that the hysteresis is proportional to the excitation amplitude for both systems at these resonant frequencies.

The fits results are:

EMAS GAIN = 0.00

Maraging Hysteresis: (3.88 ± 0.12)% of mm in the filter position for a filter tuning of 0.764 Hz.

Glassy metal Hysteresis: (1.30 ± 0.05)% of mm in the filter position for a filter tuning of 0.8552 Hz.

EMAS GAIN = -0.50

Maraging Hysteresis: (3.81 ± 0.11)% of mm in the filter position for a filter tuning of 0.748 Hz.

Glassy metal Hysteresis: (1.17 ± 0.02)% of mm in the filter position for a filter tuning of 0.848 Hz.

The result seems to confirm the theoretical model adopted in this work for both the used EMAS GAIN.

Let's note the marked experimental point for the Maraging (fig. 4.12): its deviation from the fit is surely due to the fact that it is obtained through Internet connection (Timbuktu program)which gave us a not perfectly clear signal.

Despite the similarities of behavior, the most likely theoretical explanation of the observed hysteresis is different for the two materials:

MARAGING CASE

Elasticity comes from two kinds of contributions: the bulk, immutable, provided by the crystalline structure, and a smaller percentage provided by entangled dislocations. The second contribution changes with the dislocation network distribution: the location of the filter's equilibrium point depends on where the dislocations entangle and freeze. The dislocations, able to move thanks to the pulsed stresses, eventually re – entangled in a different equilibrium position: this seems to be the most helpful interpretation to explain the observed hysteresis. Our devices, the EMAS and the GAS filters, can reduce the overall restoring force, emphasizing in such a way the effect. As we have already said, the two filters represent our personal microscope to investigate the properties of the materials. The effect dramatically enhances at low frequencies because the restoring force of the crystal lattice structure is almost nulled by the EMAS mechanism. The role of the temperature is fundamental: temperature variations can affect the internal stresses and change the dislocation landscape, providing the energy for avalanches that

can be triggered by other mechanisms, as well as by other non-observable causes like tilts, vibrations etc…In the GAS vertical springs, even if the dislocation landscape is flattened, the temperature fluctuations can later tilt it, restarting the avalanches process and generating the equilibrium point random walk. Moreover in the case of the horizontal oscillators like Inverted Pendula, actual ground tilts play an equivalent role thus explaining the observed random walk of the VIRGO [21] and TAMA [22] IP equilibrium point.

GLASSY METAL CASE

The most convincing model about dissipation inside glassy metal blades is the formation of shear bands. According to many studies [23], strain in granular dense material, such as our LM001, is often localized in a narrow region called *shear band*. Shear bands are detached from the free surface and are entirely covered in the bulk. Strain is not distributed throughout the sample but appears in a localized and narrow interface between two essentially unstrained parts. The shear stress in the contacting surface between two particles is similar to the Coulomb friction between two solid bodies. It acts against the sliding direction, its magnitude is proportional to the normal pressure acting on the two sides, but it is independent of the sliding velocity. The shear bands, originated from many collisions and slip events, are similar to a source of small vibrations propagating in the whole system. They can cause slight creeps at the particle – wall – contacts inhibiting the particle to occupy their original position, thus explaining the observed hysteresis. Propagation of shear bands in a thin specimen of LM001 creates a step at the surface. Moreover this step changes the mass – thickness in a TEM analysis (Transmission Electron Microscopy) in the region of shear band. Shear bands appears lighter or darker compared to the surrounding material (fig. 4.14), according to the orientation of shear direction with respect to the electron beam. TEM also allows the measure of shear bands dimension: the typical width is around 120 – 200 nm and the maximum thickness measured was 10 nm. Anyway, this model is object of numerous and actual studies before to be confirmed.
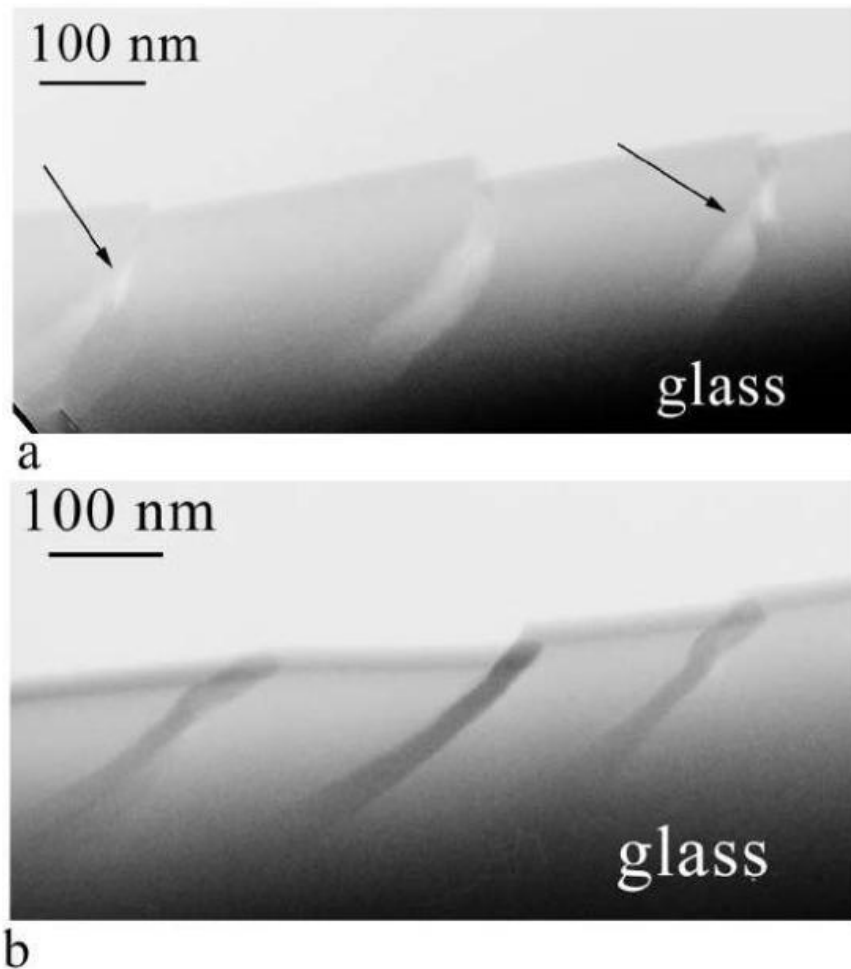
Figure 4.14: TEM shows shear bands darker(b) or lighter(a) compared to the surrounding material.

4.4 Beginning Q – factors measurements

In this paragraph we will show only the beginning of these measurements, which need more detailed study for a significant conclusion and interpretation.

We measured the resonant frequency and oscillation Q – factor ($Q = \omega\tau$, where ω and τ are pulsation and lifetime of each ring down) of both the system without feedback as they evolve during ring down. We excited the springs applying a short voltage pulse on the actuator with an EMAS GAIN = 0.00, and we saved the ring down acquired by Labview program. These measurements were done just to see the potentiality of the systems and to see if they work because, without changing the EMAS GAIN, we didn't explore different resonant frequencies. The data acquisition was generally done during the night because our presence in the laboratory (in particular the heat coming out from our bodies) had dramatic effects on the measurements. We

Chapter 4. Experimental approach and data analysis

then fitted data using a damped sinusoidal function like in the case of the working point calibration. We divided each ring down in about 10 windows, each 15/20 seconds long, spaced at 8 seconds interval. In each window we extracted the resonant frequency and lifetime with their errors.
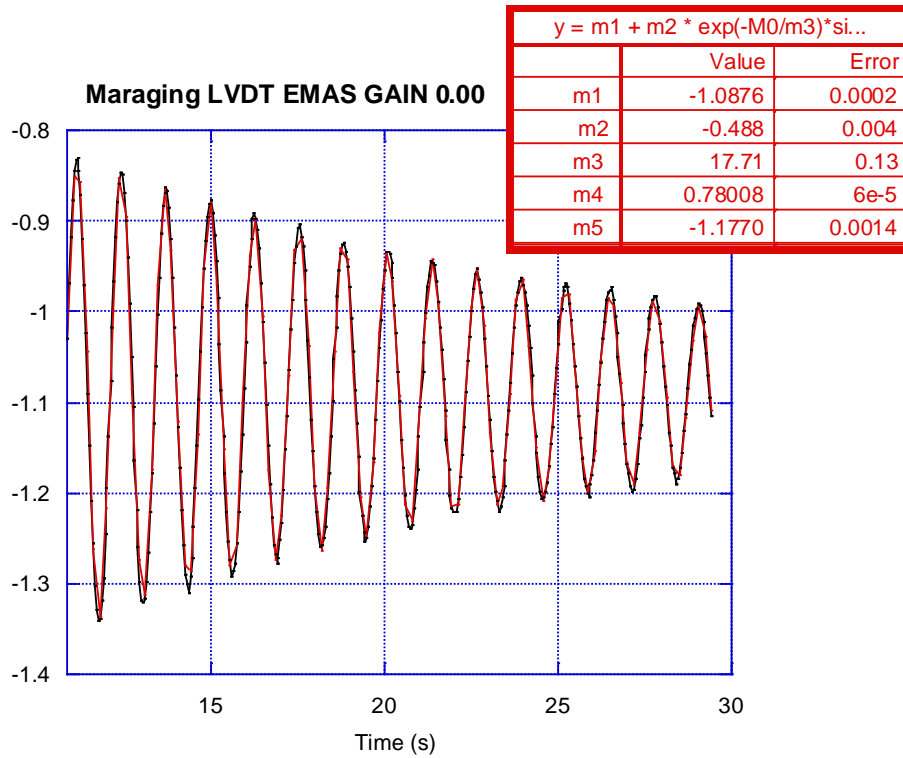

| y = m1 + m2 * exp(-M0/m3)*si...		
	Value	Error
m1	-1.0876	0.0002
m2	-0.488	0.004
m3	17.71	0.13
m4	0.78008	6e-5
m5	-1.1770	0.0014

Maraging LVDT EMAS GAIN 0.00

Figure 4.15: Example of an extracted window and the sinusoidal damped fit to it connected. The lifetime corresponds to the parameter m3, while the resonant frequency to the parameter m4.

Plotting Q – factor versus Frequency we obtained :

Q FACTOR VS FREQUENCY MARAGING EMAS GAIN 0.00

Frequency (Hz)

Q FACTOR VS FREQUENCY GLASSY EMAS GAIN 0.00
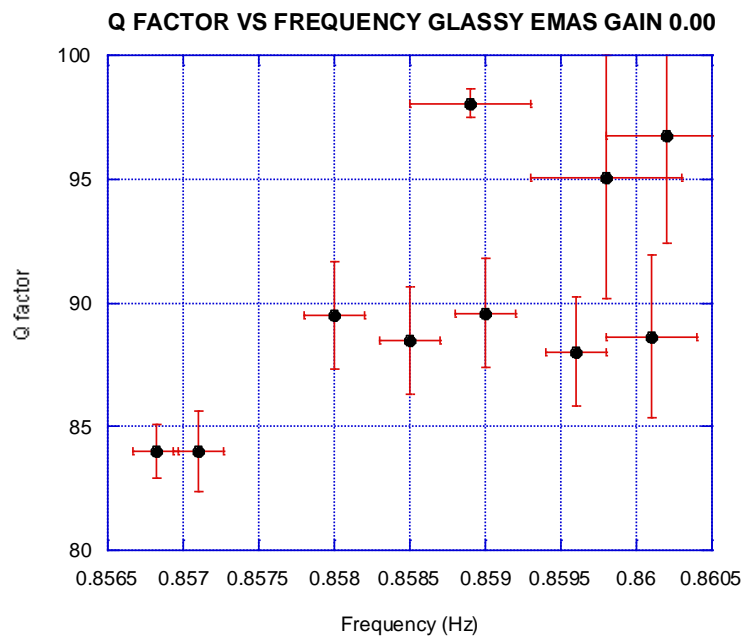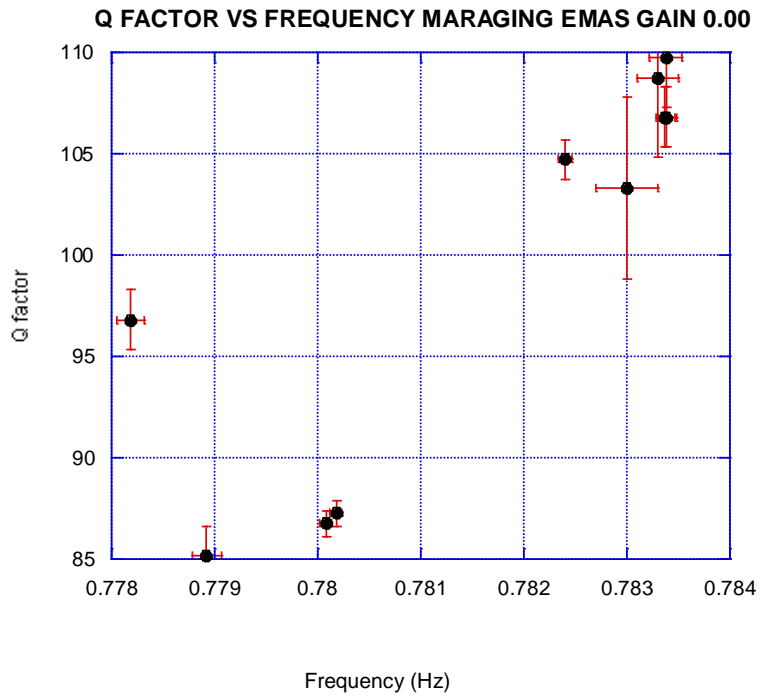
Frequency (Hz)

Being the Q factor defined as the energy stored in the system divided by the energy dissipated per cycle, it is clear that it should follow a quadratic function of frequency if the losses per cycle are frequency independent, i.e. if

we are in a purely hysteretic regime, that is our Maraging case. In the Glassy metal case the result is an interesting still open question.
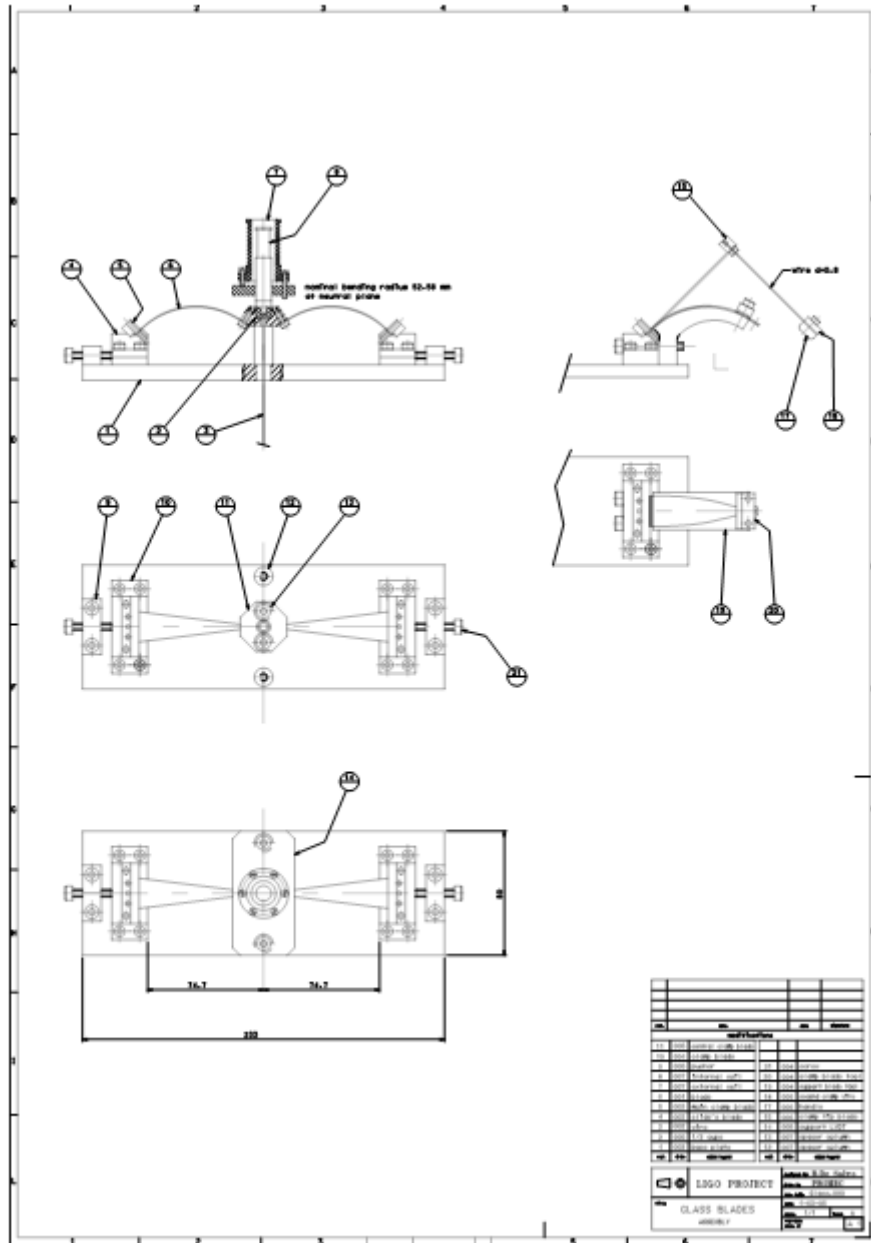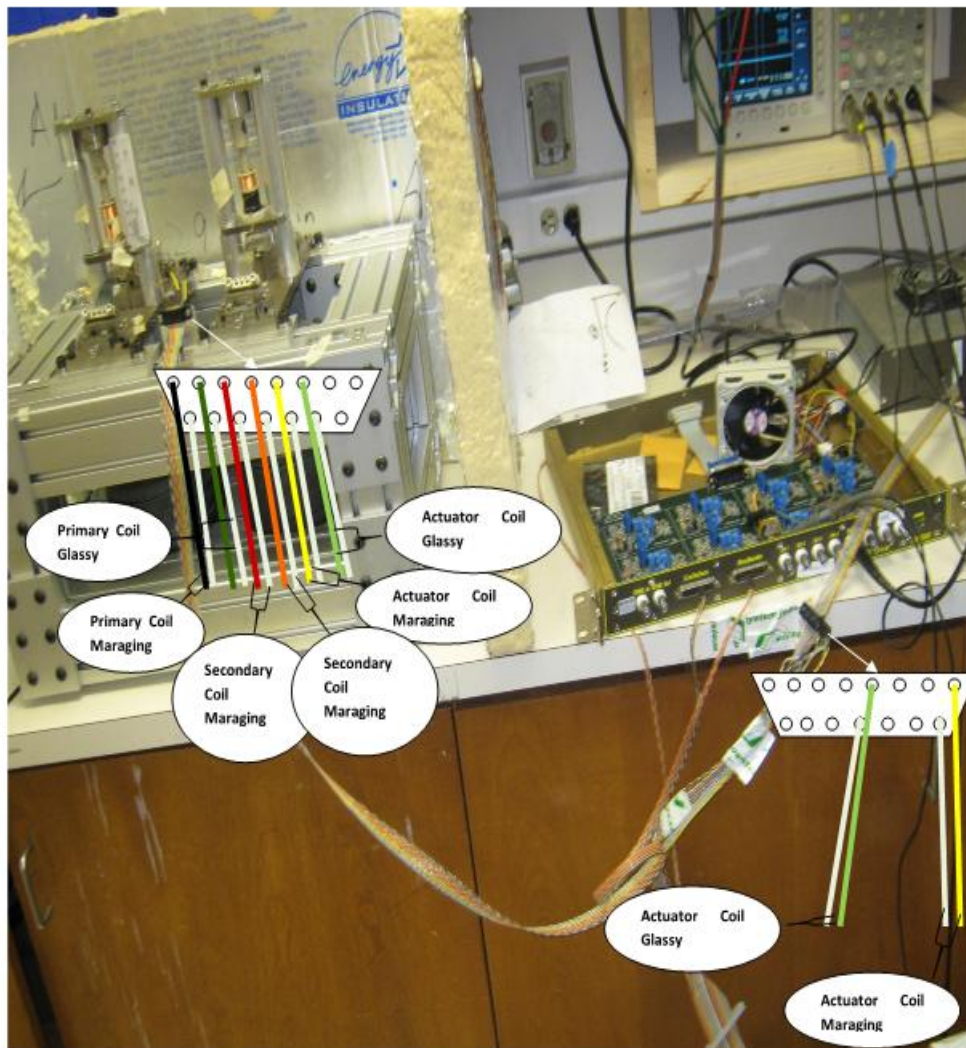
Chapter 5

Conclusions and future prospects

The goal of this thesis work was to explore new materials for the future, third generation, Gravitational Waves interferometer detectors of the future third generation. In particular way I focused on the actual adopted material, Maraging Marval $-$ 18, and LM001, a very interesting material for both research and engineering activity. The result obtained seem to agree with the theoretical model from which we started our analysis. Considering first an EMAS GAIN = 0.00, which corresponds to a $k_{EMAS} = 0.00$ for both the systems, we found that Maraging hysteresis was about three times that of the Glassy metal prototype. Later we used an EMAS GAIN = $-$ 0.50 corresponding to a $k_{EMAS} = (-8.6 \pm 0.3)$ *N/m* for the Maraging and to a $k_{EMAS} = (-8.2 \pm 0.2) N/m$ for the BMG, founding Maraging hysteresis 3.2 bigger than Glassy metal one. For both the EMAS GAIN the results follow our hypothesis: dislocations are responsible of the dissipation properties inside the materials, therefore, a material which don't contain them (our LM001), should show lower hysteresis. Anyway, the observed hysteresis for the BMG must have another origin. The most convincing possibility is the formation of shear bands and the propagation connected to them. However they need to be deeply studied to formulate a complete theoretical model about dissipation inside the BMG. An helpful device could be the continuation of this compared study with other different EMAS GAINS to see if at lower frequencies the scenario changes or it persists. It could be more physically interesting comparing the two systems not at the same EMAS GAIN, but at the same resonant frequency. Moreover it is necessary to acquire a huge number of experimental points to fit Q factor versus frequency to confirm the Maraging results obtained in other works and to explore the new material, for which each expectation is still open. Moreover could be interesting to start a creep test, similar to that performed for Maraging, (about ten years ago) for the LM001 considering the specific stress to which the blades are subjected in a GAS filter, in such a way to have a complete comparative overview between the two materials.
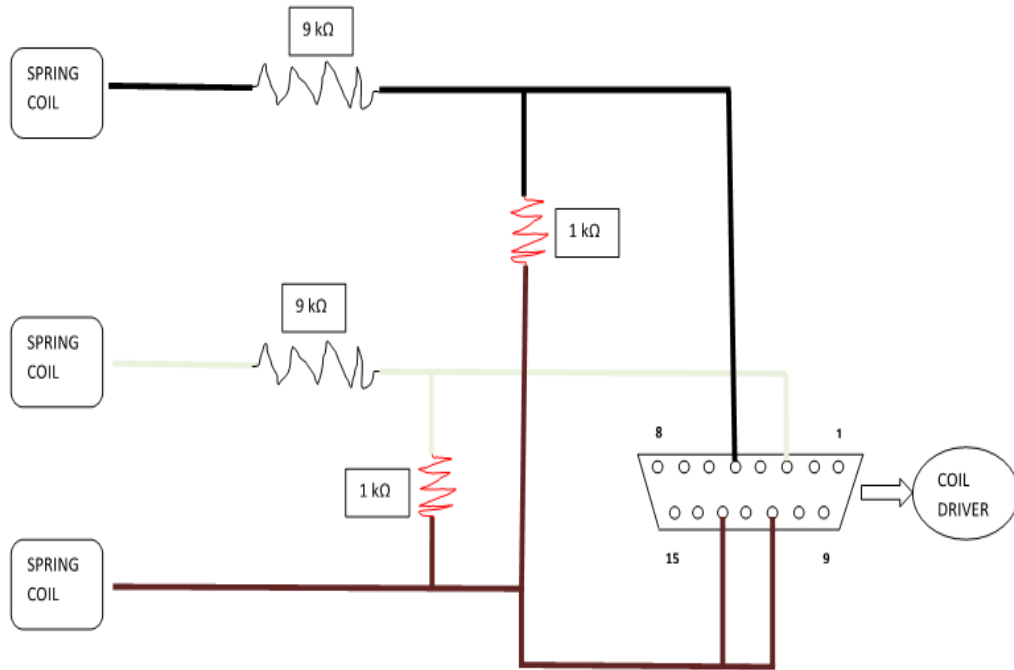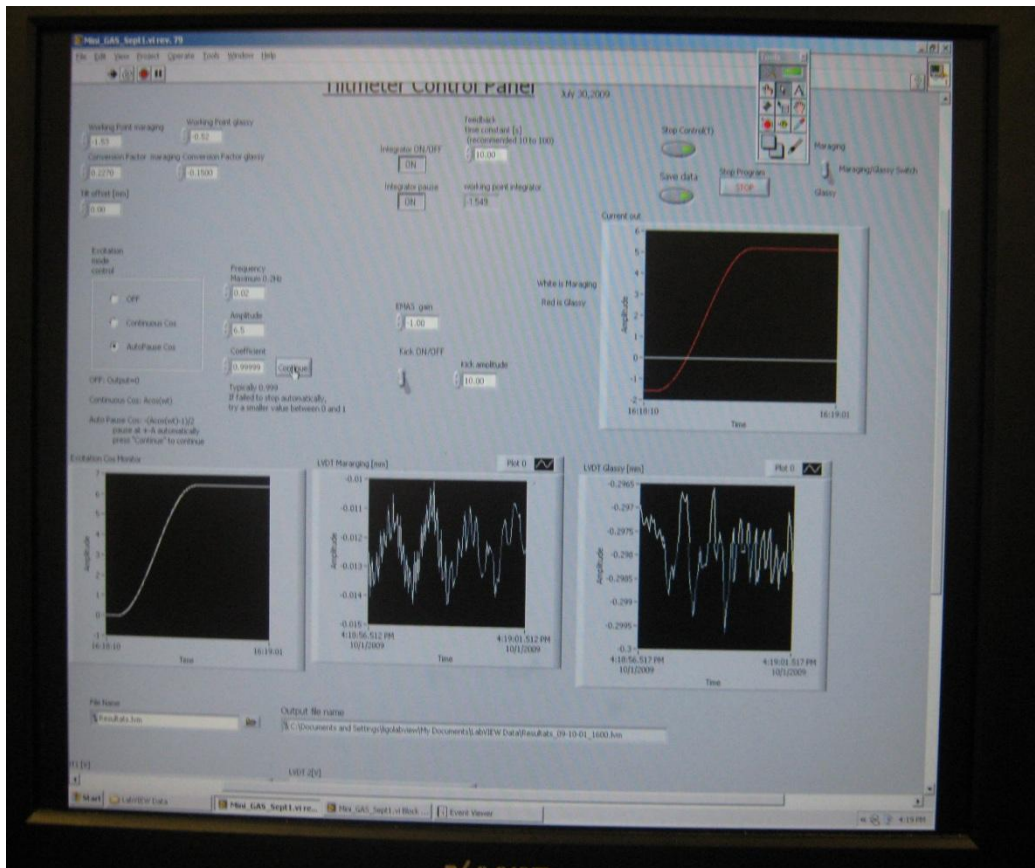
Appendix

Glassy blades Assembly: drawing

Connections diagram of the experiment with the same colors of the wiring.

Scheme to reduce the digitalization noise

Control panel of the Labview program adopted

Bibliography

[1] J. H. Taylor, *Binary pulsars and relativistic gravity*, Rev. Mod. Phys., 66, 711, (1994).

[2] R.A. Hulse, *The discovery of the binary pulsar,* Rev. Mod. Phys., 66, 699 (1994).

[3] Vincenzo Rubino, *Studio del microcreep nelle sospensioni degli specchi di VIRGO*, thesis work (1997).

[4] Massimo Granata, *Ultimo stadio criogenico di sospensione per interferometri di terza generazione per la rivelazione di onde gravitazionali*, master thesis, chapter 2, p. 2.2.1 (2008).

[5] LIGO project, www.ligo.caltech.edu

[6] VIRGO project, www.virgo.infn.it

[7] DUSEL (Deep underground Gravity Laboratory), Final Proposal (2009).

[8] Arianna Di Cintio, *Astrophysics issues and low frequency mechanical noise for third generation Gravitational Waves detectors*, master thesis (2009).

[9] Arianna Di Cintio, Fabio Marchesoni, Maria Ascione, Abhik Bhawal and Riccardo De Salvo, *Dislocation movement and hysteresis in Maraging blades*, Class. Quantum gravity, 26 204018 (2009).

[10] A. Stochino et al, *The SAS Seismic Attenuation System for the Advanced LIGO Gravitational Waves Interferometers Detectors*, Nucl. Instrum. Methods Phys. Res. A, 598, 737 – 753 (2008).

[11] J. P. Hirth and J. Lothe, *Theory of Dislocations,* McGraw – Hill New York (1968).

[12] F. Marchesoni and M. Patriarca, *Self – Organized Criticality in Dislocation Networks*, Phys. Rev. Lett. 72, 4101 (1994).

[13] G. Y. Wang et al, *Comparison of fatigue behavior of a bulk metallic glass and its composite,* Volume 14, Issues 8 – 9 pages 1091 – 1097, Fourth International Conference on Bulk Metallic Glasses (2006).

[14] P. Bak et al, *Self organized criticality: An explanation of the 1/f noise*, Phys. Rev. Lett. 59, 381 – 84 (1987).

[15] R. De Salvo, *Passive, Nonlinear, Mechanical Structures for Seismic Attenuation*, J. Comput. Nonlinear Dynam. 2, 290 – 298 (2007).

[16] Akiteru Takamori, *Low frequency Seismic Isolation for Gravitational Wave Detectors,* thesis work (2002).

[17] A. Stochino, *The HAS – SAS Seismic Isolation System for the Advanced LIGO Gravitational Wave Interferometers,* master thesis, (2006 – 2007).

[18] M. Mantovani and Riccardo De Salvo, *One hertz seismic attenuation for low frequency gravitational waves interferometers,* Nucl. Instrum. And Meth., 554, 546 – 554 (2004).

[19] Hareem Tariq et al, *The linear Differential Transformer (LVDT) position sensor for Gravitational Wave Interferometer low – frequency controls*, Nucl. Instrum. And Meth., 489, 570 – 576 (2002).

[20] Chenyang Wang et al, *Constant force actuator for gravitational wave detector's seismic attenuation system (SAS)*, Nucl. Instrum. And Meth., 489, 563 – 569 (2002).

[21] P. Ruggi, VIRGO project, private comm.

[22] K. Arai, TAMA project, private comm.

[23] T. Unger et al, *Shear band formation in granular media as a variation problem*, PACS numbers 45 – 70 (2008).